7

Electron Spin Resonance Characterization of Microporous and Mesoporous Oxide Materials

Larry Kevan[†]
University of Houston, Houston, Texas, U.S.A.

I. ELECTRON SPIN RESONANCE BACKGROUND

Electron spin resonance (ESR) or electron magnetic resonance is a type of magnetic resonance spectroscopy that deals with transitions between magnetic energy levels associated with different orientations of an electron spin in an atom or molecule, generally in an external magnetic field. Measurement of the allowed transitions between the electron magnetic energy levels produces a spectrum of an atomic or molecular system with net electron spin angular momentum. Generally such systems are defined as those having one or more unpaired electrons. Analysis of the ESR spectrum can give information about the identification of the species, the geometrical structure, the electronic structure, and the internal or overall rotational or translational motion of the species. The most common types of systems studied are free radicals, which can be regarded as atoms or molecules containing one unpaired electron, and transition metal ion and rare-earth ions. The specificity of ESR spectroscopy for species containing unpaired electrons is particularly valuable for the study of chemical reaction intermediates.

Experimentally it is found that isolated electrons in a magnetic field absorb a quantized amount of energy, which means that they must have at least two energy levels. These are not translational energy levels because the amount of energy absorbed does not depend on the kinetic energy of the electron. However, the magnitude of the energy absorbed does depend on the magnitude of the magnetic field to which the electrons are exposed. To explain the existence of these magnetic energy levels, it is postulated that an electron has an intrinsic angular momentum, called spin angular momentum. When this spin angular momentum interacts with a magnetic field, two different energy levels are produced whose difference accounts for the absorption of energy by the unpaired electron system.

The Hamiltonian energy operator for the electron spin transition we have just discussed is given by:

$$\mathcal{H}_{\text{spin}} = \text{gh}\boldsymbol{S} \cdot \boldsymbol{H} \tag{1}$$

[†] Deceased.

where $\mathcal{H}_{\text{spin}}$ is the spin Hamiltonian energy operator. $\boldsymbol{S}$ is the spin angular momentum, $\boldsymbol{H}$ is the magnetic field, and $g\beta$ is a proportionality constant where $g = 2.0023$ and is called the g factor or spectroscopic splitting factor, which is dimensionless, and β is the Bohr magneton, which has a value of 9.27×10^{-24} J/T. This spin Hamiltonian operates only on spin wave functions and not on orbital wave functions that are commonly associated with electronic energy levels. For an electron there are two spin wave functions, typically denoted by a and b, which are characterized by$+1/2h$ and $-1/2h$ where h is Planck's constant divided by 2π and gives the unit of spin angular momentum. The two energy levels associated with an electron in a magnetic field are thus given by $+1/2\ g\beta H$ and $-1/2\ g\beta H$. The difference between these two energy levels is gβH, so that the transition energy is given by $h\nu = g\beta H$.

Typically, electron magnetic resonance is carried out in a magnetic field of about 3000 G (gauss) or 0.3 T (tesla). This corresponds to an energy absorption frequency of about 9 GHz. This frequency is in the microwave range. As for any spectral transition, the number of systems or electrons in the upper and lower energy states at thermal equilibrium is given by a Boltzmann distribution.

The real power of ESR spectroscopy for structural studies is due to interaction of the unpaired electron spin with nuclear spins in molecular species. This gives rise to a splitting of the energy levels and generally allows the determination of the atomic or molecular structure of the radical species. In this situation the spin Hamiltonian of Eq. (1) involves additional terms corresponding to the nuclear spin interacting with the magnetic field, to the nuclear spin interacting with the electron spin, and, if the nuclear spin is ≥ 1, to a nuclear quadrupole interaction. This more complete spin Hamiltonian may be written as follows:

$$\mathcal{H}_{\text{spin}} = \beta \boldsymbol{H} \cdot \mathrm{g} \cdot \boldsymbol{S} + \sum_{\mathrm{n}} \mathrm{H}\boldsymbol{S} \cdot \mathrm{A_n} \cdot \boldsymbol{I}_{\mathrm{n}} - \sum_{n} g_{\mathrm{n}} \beta_{\mathrm{n}} \boldsymbol{H} + h \sum_{n} \boldsymbol{I}_n \cdot Q_n \cdot \boldsymbol{I}_n \tag{2}$$

In Eq. (2) the summations are taken over all of the nuclei in the molecular species. The new symbols in Eq. (2) are defined as follows: g_{n} is the nuclear g factor, which is dimensionless; β_{n} is the nuclear magneton, having units of joules per gauss or per tesla; the nuclear spin angular momentum operator $\boldsymbol{I}_{\mathrm{n}}$; the electron-nucleus hyperfine tensor $\mathrm{A_n}$; the quadrupole interaction tensor Q_{n}; and Planck's constant h.

The general spin Hamiltonian is given by Eq. (2), in which the interaction parameters are written in the general tensor form. The components of the diagonalized hyperfine tensor consist of an isotropic part A_0 with three identical principal values and a purely anisotropic part A', with three principal values whose sum (orientational average) is zero. The theoretical expression relating the isotropic hyperfine coupling constant for atoms is given by

$$hA_0 = (8/3)\pi g \beta g_{\mathrm{N}} \beta_{\mathrm{N}} |\psi(0)|^2 \tag{3}$$

where the units are joules on both sides of the equation and $|\psi(0)|^2$ is the probability density of the electron being at the nucleus. From a quantum mechanical point of view, the unpaired electron is in contact with the nucleus, and hence the isotropic hyperfine coupling is called a ''contact'' interaction. Only s orbitals have finite electron density at a nucleus; p, d, and f orbitals all have nodes at the nucleus. Thus, contact interaction depends on the s-electron character of the unpaired electron, and the hyperfine constant for a given nucleus provides a measure of the contributions of the s orbitals on the corresponding atom to the total many-electron wavefunction of the atom or molecule.

The physical interpretation of the principal values of the anisotropic part of the hyperfine tensor is given by the classical magnetic dipolar interaction between the electron and nuclear spin angular momenta. This interaction energy is given by

$$\mathcal{H}_{\text{aniso}} = -\text{ghg}_{\text{N}}\text{h}_{\text{N}}\left|\frac{1-3(\cos^2\phi)}{r^3}\right|I\cdot S \tag{4}$$

where r is the vector between the unpaired electron and the nucleus with which the interaction occurs and ϕ is the angle between r and the electron spin angular momentum vector S, which is in the direction of the external magnetic field. The A′ principal values are given by

$$A' = -g\beta g_{\text{N}}\beta_{\text{N}}h^{-1}\left|\frac{1-3(\cos^2\phi)}{r^3}\right|av \tag{5}$$

where *av* denotes a spatial average over the electronic orbital of the unpaired electron. The three components of A' are given by three different values of the angular average of corresponding to rotation in three mutally perpendicular planes of the principal axis system.

The dipolar function $[1 - 3(\cos^2\phi)/r^3]_{av}$ can be evaluated from known wavefunctions of electrons in s, p, d, etc., orbitals on different atoms. For s orbitals the dipolar function is zero because of spherical symmetry. The cylindrical symmetry of p orbitals gives three components, $A'_{\parallel}$, $A'_{\perp}$, and $A'_{\perp}$, which are related by $A'_{\parallel} = -2A'_{\perp}$. Note that the dipolar angular function changes sign at $\phi = 54°44''$. Thus, the space around a nucleus can be divided into four regions alternating in sign. In the determination of the hyperfine tensor, a set of signs of the components will be obtained so that the sum of the diagonal principal values is zero.

In the general spin Hamiltonian given by Eq. (2), the *g* factor given in the electron Zeeman energy term is written as a tensor connecting the electron spin angular momentum operator ***S*** and the magnetic field vector ***H***. A free electron has *only* spin angular momentum, and its orientation in a magnetic field is determined only by this physical property. However, in general, in atomic and molecular systems there will be some contribution from orbital angular momentum to the total unpaired electron wavefunction. In this case, the orbital and spin angular momentum vectors interact, and by convention this interaction is incorporated into an "effective" anisotropy in the *g* factor. In this representation the spin angular momentum vector ***S*** no longer represents "the true spin" because the true spin has only spin angular momentum and is associated with an isotropic *g* value. Instead, when *g* is written as a tensor the spin angular momentum vecor represents an effective spin, which instead of being oriented along the magnetic field direction is oriented along the vector $\boldsymbol{H}\cdot g$. For most purposes this nuance will not affect our utilization of the *g*-tensor formulation.

The general experimental determination of the *g* tensor is carried out by a procedure analogous to that for determination of the anisotropic hyperfine tensor for a single crystal sample. Measurements are required as a function of angle in three mutually perpendicular planes. From this data, a general g tensor is obtained, which is diagonalized to find the principal values. The principal axes of the *g* tensor are often the same as for the hyperfine tensor, but they do not have to be.

The interpretation of the principal values of the *g* tensor can be conveniently discussed by Eq. (6).

$$\text{g}_{\text{obs}} = \text{g}_{\text{e}} + \frac{C\lambda}{\Delta E} \tag{6}$$

In this expression g_{e} is the *g* factor for an isolated spin (2.0023), λ is the spin-orbit coupling constant, *C* is a proportionality constant calculated from the electronic wave functions, and ΔE is the energy difference between the ground state and the first excited state. Values of λ have been

obtained for a number of atoms and ions from atomic spectra, but the particular value to be used in a molecular system can only be approximated by this. In general, g values increase with atomic number. The values of ΔE can sometimes be deduced from electronic spectra. Thus, the g anisotropy is related to the electronic wavefunction, and if sufficient information is known about the electronic wavefunction the principal λ components can be calculated and compared with experiment. The difficulty is that information about the excited-state energy levels need to be known to properly calculate the g tensor and this is only generally known for simple molecular systems. In a few cases, such as for the CO_2^- radical ion, detailed calculations have been carried out and the experimental g anisotropy has given information about the molecular wavefunction.

The largest g anisotropy occurs for transition metal ions, where the g anisotropy is very useful for discriminating between transition metal ions in different types of environments. The range of g anisotropy can be rather large. Typical values for axial g anisotropy range from $g_\perp = 2.04$ and $g_\parallel = 2.17$ for copper complexes to $g_\perp = 6$ and $g_\parallel = 2$ for some ferric complexes.

II. PULSED ELECTRON SPIN RESONANCE BACKGROUND

Transient spin echoes are produced in response to suitable resonant microwave pulse sequences in magnetic resonance. The pulse sequences reorient the magnetic dipoles such that they dephase and rephase while subject to all time-dependent magnetic interactions in the system. The rephasing of the magnetic dipoles to reform macroscopic magnetic moments constitutes the echo. A two-pulse sequence involves a 90° pulse followed by a 180° pulse followed by the echo at the same interpulse time after the 180° pulse. As the time between the two pulses (τ) is varied, the echo amplitude traces out a decay envelope, which may be modulated due to weak electron-nuclear hyperfine interactions. Analysis of this modulation affords a way to measure weak hyperfine interactions and allows determination of the number and distance of these interacting magnetic nuclei. This pulsed ESR method is called electron spin echo modulation (ESEM) (1,2) or electron spin-echo envelope modulation (ESEEM).

Two-pulse and three-pulse echo sequences are most commonly used. In the three-pulse sequence the second 180° pulse of a two-pulse sequence is essentially divided into two 90° pulses. This means that there are two experimentally controllable times in the experiment, τ between the first and second pulses and T between the second and third pulses. It is therefore possible to suppress one nuclear modulation frequency by appropriate selection of one of these times. This allows us to study hyperfine interactions of adsorbate molecules relative to a paramagnetic probe while suppressing hyperfine interactions with framework nuclei. It is also possible to easily see deuterium modulation while suppressing protium modulation when both nuclei are present in the same molecule by selecting the proper pulse amplitude. This occurs because of the significant difference in the nuclear frequency of protons versus deuterons. This is quite useful because it allows the determination of the *orientation* of an adsorbed molecule with respect to a paramagnetic probe by using selective deuteration in different parts of the molecule. An example is methanol adsorbate in which the hydroxyl or the methyl group can be deuterated, and thus distances to two different positions in the methanol molecule can be measured.

In a disordered system one determines an average structure by a spherical approximation analysis (3,4) of the ESEM pattern which primarily involves the nearest magnetic nuclei surrounding the paramagnetic species. When more than one molecule is arranged equivalently around the paramagnetic species in the first solvation shell, an average structural analysis of this type is valid if the nearest nuclear distances are greater than about 0.25 nm. If there are magnetic nuclei that are close enough to give detectable magnetic interactions and they are arranged in more than one shell around the solvated species, they can be resolved in favorable circumstances. The general simulation procedure is to analyze the spin-echo modulation pattern in

terms of a number N of equivalent magnetic nuclei located at a distance R from the paramagnetic species with a small overlap of the unpaired electron wavefunction on the closest nuclei to give isotropic hyperfine coupling A_0.

The basic simulation procedure in the absence of quadrupole interaction is well developed (5,6). Three approximations typically made for application to powder systems are the point dipole approximation for the dipolar hyperfine interaction, the spherical approximation for averaging over N uncorrelated nuclei, and neglect of the quadrupole interaction. The point dipole approximation is generally adequate for transition metal ions in oxides. In disordered systems, where ESEM analysis has been most widely used, one must average over all orientations. For N equivalent nuclei arranged in a known geometry the explicit angular correlation can be incorporated before orientational averaging. However, for the typical disordered experimental system the explicit nuclear geometry is unknown. So a spherical approximation was developed involving three-dimensional averaging assuming uncorrelated nuclei (3), which has been widely used with satisfactory results and has undergone detailed evaluation (7,8). Thus, in disordered systems where essentially nothing is known about the nuclear geometry surrounding a paramagnetic species, significant information can be obtained about the number of nearest interacting nuclei at distance R from an ESEM analysis.

It is not difficult to formally include a quadrupole interaction in the Hamiltonian used for simulation of echo modulation patterns. However, this introduces several additional parameters that must be determined by the fit of simulated patterns to experimental patterns. Especially in the time domain, the sensitivity of the pattern in the presence of large quadrupole interactions is often insufficient to determine a particular set of magnetic parameters. However, for the much studied case of deuterium modulation the quadrupole interaction is relatively small. Therefore, its neglect can be reasonably well justified for analysis over interpulse times less than about 2 μs. At longer interpulse times for both two- and three-pulse echoes, deuterium modulation can have significant effects. Several approximation methods involving perturbation theories have been developed to account for the quadrupole interaction effect on the time domain ESEM pattern (9–12).

More recent developments in the practical applications of ESEM spectroscopy involve HYSCORE (13) and pulsed electron nuclear double resonance (ENDOR) (14,15). There are not new methods, but only recently have practical applications been developed (16). HYSCORE is an acronym for hyperfine-sublevel correlation experiment and uses a four-pulse sequence, which is like the three-pulse sequence with an additional π pulse introduced within the second interpulse period T. T is then divided into two periods, t_1 after the second pulse before the π pulse and t_2 after the π pulse to the end of period T. The HYSCORE experiment is a two-dimensional experiment because the echo is recorded as a function of both t_1 and t_2 where these two times are not equal. Fourier transform is carried out with respect to both t_1 and t_2. In HYSCORE the spectrum exhibits cross peaks only between nuclear frequencies corresponding to different electron spin manifolds. The intensity of the cross-peaks is a complex function of the hyperfine interaction, but they are symmetrical with respect to the diagonal of the two time axes. The advantage of HYSCORE is that the resolution is improved since the spectrum is spread over two dimensions instead of one, and most importantly, that it provides correlations that are important and sometimes essential for proper ESEM frequency assignments. This is particularly true when several coupled nuclei are present and when the nuclear spin is greater than one.

ENDOR is an important continuous wave (CW) magnetic resonance technique. Recently it has also been developed as a useful pulsed technique. ENDOR simply involves the simultaneous application of electron and nuclear resonance frequencies to a sample with detection via the ESR transition. In CW ENDOR a particular ESR transition is saturated with high microwave power

while the radiofrequency is swept. When a nuclear magnetic resonance transition matches the radiofrequency, it causes a desaturation of the ESR transition. An increased ESR signal appears that is detected as an ENDOR response. The CW ENDOR response depends sensitively on the balance of various magnetic relaxation processes. One advantage of pulsed ENDOR is that it is free of this limitation and one is more generally able to detect pulsed ENDOR signals. This allows one to simplify spectra and to detect particular hyperfine transitions.

Two common pulse sequences are used for pulsed ENDOR. The Mims ENDOR sequence is a three-pulse sequence in which a radiofrequency π pulse is introduced during the second microwave pulse sequence time interval T (14). When the radiofrequency matches a nuclear transition the intensity of the echo changes, which is a pulsed ENDOR response. A Mims ENDOR sequence is most useful for systems with weak nuclear coupling. A second ENDOR sequence, called Davies ENDOR, is effective for larger hyperfine coupling (15). In Davies ENDOR a radiofrequency π pulse is applied after an initial microwave π pulse with subsequent $\pi/2$ and π microwave pulses. In general, pulsed ENDOR experiments are tricky and signals may not be observed due to short spin lattice relaxation time or other factors. Also the instrumentation is complex and more expensive. Nevertheless, ENDOR is very useful when it can be applied because of the specificity of the information that can be obtained (16).

III. APPLICATIONS TO PARAMAGNETIC METAL IONS IN MICROPOROUS AND MESOPOROUS OXIDE MATERIALS

In this section we will give several case studies concerning the use of electron magnetic resonance involving metal ions in these materials. Initially, we will consider some examples with zeolites. A first question is, where is the cation located within a zeolite and how can this be controlled? Control is important if the cation is an active site for a catalytic reaction. A second question is how is the cation coordinated to absorbates and how can this be controlled? This involves the possible detection of catalytic reaction intermediates. A third question is, how are the cation location and geometry related to its catalytic activity or efficiency?

A. Determination of Ion Location

The first case study involves the location of a cupric ion in zeolite A (17). The structure of zeolite A showing the cation sites is given in Fig. 1. Cupric ion is paramagnetic and it is substituted to a very small extent for Cs^+ in Cs-A zeolite. Electron spin-echo modulation involving the interaction between the cupric ion and the cesium nuclei generates ^{133}Cs modulation, which is then analyzed to determine the location of the cupric ion. Based on previous studies it is known that the most probable site for Cu^{2+} to substitute by ion exchange for Cs^+ is near an S2 site as shown in Fig. 1. Site S2 is in a 6-ring between the small beta cage and the large alpha cage of A zeolite. Sites S2′ and S2* are displaced from the S2 site into the beta cage (S2′) and into the alpha cage (S2*).

Figure 2 shows the cesium modulation that is expected for a cupric ion in site S2 and displaced at two distances into the alpha cage, which would be a S2* site, and displaced at two distances into the beta cage, which would be a S2′ site. One can see that the ^{133}Cs modulation depth is quite sensitive to the location of the cupric ion. This model is based on interaction with three cesium ions, which are quite large ions and are known to be located by X-ray diffraction at site S5. One cannot locate the copper ion by x-ray diffraction because its concentration is too small.

One can see that the cesium modulation depth is larger for the copper located in the alpha cage where it is closer to cesiums at site S5. The modulation depth also shows that the sensitivity to distance is good enough to locate the cupric one to about 0.01 nm. An ESR spectrum can be observed by detecting the echo at a given interpulse time and sweeping the

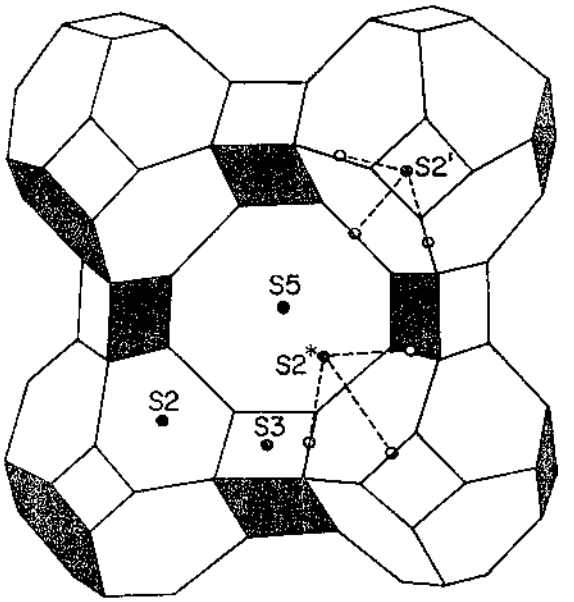

Fig. 1 Crystal structure of zeolite A showing cation positions. Site S2 is at the center of a six-ring face with site S2′ and S2* displaced into and out of the β cage along the triad axis, respectively. Site S3 is adjacent to the 4-ring in the α cage while site S5 is at the center of the octagonal window. (From Ref. 17.)

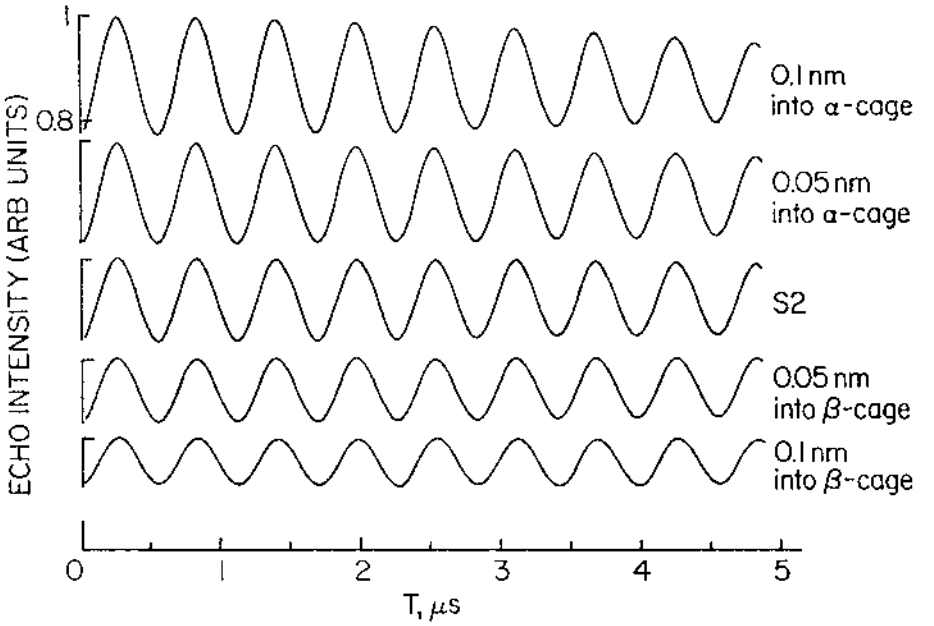

Fig. 2 Theoretical three-pulse ESEM spectra for Cu^{2+} cation located on the triad axis near site S2 and interacting with three nearest-neighbor cesium cations. (From Ref. 17.)

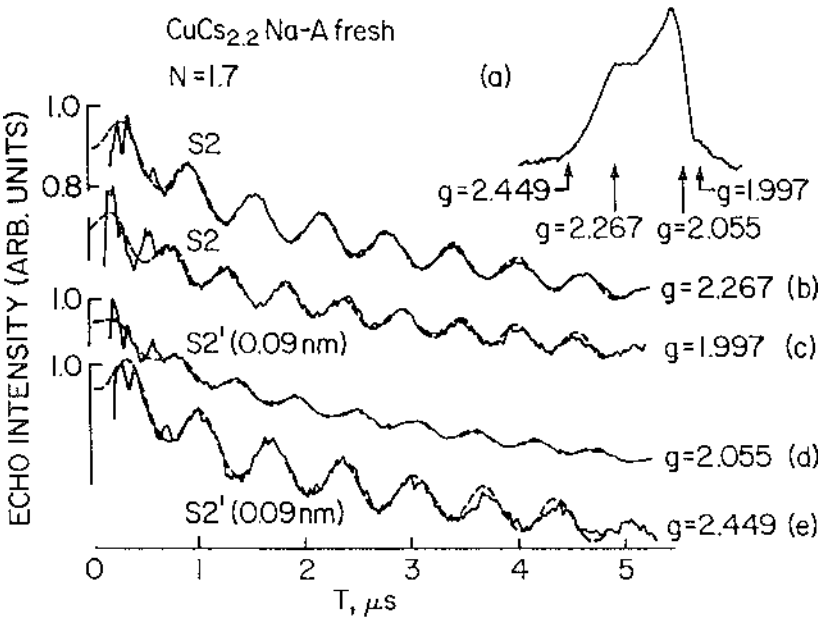

Fig. 3 (a) Field-swept ESEM spectrum of fresh $CuCs_{2.2}Na$-A. Experimental (——) and simulated (----) three-pulse ESEM spectra of fresh $CuCs_{2.2}Na$-A recorded at 4 K and at (b) $g_\perp = 2.266$ and (c) $g_\parallel = 1.997$ for Cu^{2+} coordinated to two waters and at (d) $g_\perp = 2.055$ and (e) $g_\parallel = 2.449$ for Cu^{2+} coordinated to three waters. Distances in brackets indicate displacement of Cu^{2+} from S2. (From Ref. 17.)

magnetic field. This produces an echo-induced ESR spectrum, which is shown in Fig. 3. It can be seen that there are two sets of g anisotropic parameters corresponding to two different cupric ion sites. By dehydrating the CuCs-A and rehydrating with deuterated water, one can analyze the two-dimensional ESEM modulation to distinguish these sites structurally by setting the magnetic field at the two $g_\perp$ positions corresponding to the two copper sites. One finds that the site with $g_\perp = 2.07$ corresponds to copper coordinated to two water molecules, which is denoted as Cu_{II}. The other copper site at $g_\perp = 2.05$ corresponds to copper coordinated to three water molecules denoted as Cu_{III}. Now the copper location for each of these sites can be determined by analyzing the cesium modulation, as shown in Fig. 3. The modulation for the Cu_{II} species corresponds to the cesium modulation depth for an S2 site in the 6-ring between the alpha and beta cages. This site is consistent with the coordination of cupric ion to only two water molecules and to three oxygens of the 6-ring to give a trigonal bipyramidal structure. This structure is also supported by the so-called reversed g-value order of $g_\perp > g_\parallel$. This means that one water coordinated to Cu(II) extends into the alpha cage and the other water extends into the beta cage, with Cu(II) also coordinated to three oxygens of the 6-ring. So the cupric ion location determined from the cesium modulation is totally consistent with the adsorbate geometry of the cupric ion.

The other cupric ion site corresponding to $g_\perp = 2.055$ has shallower cesium modulation and corresponds to cupric ion displaced into the beta cage and hence in an S2′ site. The matching of the simulated modulation with the experimental modulation corresponds to a distance of 0.09 nm extension into the beta cage.

This example shows quite clearly the power of electron spin-echo modulation for determining the location of a metal ion that is substituted in very low abundance into a zeolite as long as there is an appropriate nuclear modulation to analyze. It is also necessary to know the

location of the nuclei that produce the nuclear modulation. In this case, the cesium ion positions at S5 in A zeolite are known by X-ray diffraction. In other materials, such as microporous aluminophosphate materials, analysis of the ^{31}P modulation is particularly useful in determining the location of an ion-exchanged or framework-substituted paramagnetic ion. One might also think that the ^{27}Al modulation could be analyzed. This is true, but it is complicated by a large quadrupole interaction that adds additional parameters so that analysis of aluminum modulation has not been as useful as analysis of phosphorus modulation in determining the location of a particular metal ion site.

B. Determination of Adsorbate Geometry

The second case study of how electron magnetic resonance can be used to study aspects of zeolites and other microporous or mesoporous materials involves the determination of adsorbate geometry. The most powerful procedure has been to use partially or fully deuterated adsorbates and analyze deuterium modulation to determine the number of closest interacting deuteriums and consequently the number of directly coordinated molecules (18). Typically one analyzes first-shell molecules but in some cases one can detect two shells of deuteriums.

For specifically deuterated adsorbates one can determine the orientation of the adsorbate. For example, with methanol as absorbate one can look at the orientation of the methanol by analyzing the deuterium modulation for deuteration of the hydroxyl proton and separately for deuteration of the methyl group (19). The two distances to the specific deuteriums and the known geometry of methanol enables determination of the orientation of the methanol relative to a paramagnetic ion that it solvates. Adsorbate deuteration thus enables determination of the number of equivalent coordinated adsorbates, the probable adsorbate geometry, and in some the cases adsorbate orientation.

The following example shows how the absorbate geometry can be controlled by thermal means and can be detected by electron of spin-echo modulation analyses (20). This example involves ion-exchange of cupric ion into ZSM-5 zeolite, which has an intersecting channel type of structure. In this case, the ZSM-5 zeolite has an Si/Al ratio of about 30 with sodium ions and protons as charge-compensating ions. Into this ZSM-5, a small amount of cupric ion was incorporated by ion exchange. One interesting aspect, since the aluminum abundance is relatively low, is that aluminum modulation was not seen by electron spin echo, which indicated, based on simulations, that the Cu^{2+} to Al distance was greater than about 0.6 nm.

Figure 4 shows how one can control the absorbate coordination geometry (20). The upper spectrum in Fig. 4a shows the deuterium modulation in a three-pulse ESEM experiment with Cu-ZSM-5 with fully hydrated D_2O. One can see that the modulation is quite deep, indicating strong interactions with deuterium. The anlaysis gives 12 deuteriums at 0.28 nm, which corresponds to a typical distance for direct solvation of a cation by water. This corresponds to six approximately equivalent waters coordinated to the cupric ion or a fully hydrated Cu^{2+} with an approximate octahedral configuration. Furthermore, such a bulky species can only be located at the ZSM-5 channel intersections where there is sufficient space for this species.

By evacuating at room temperature one can remove the waters that are least strongly coordinated to Cu^{2+}. The waters are not all equally strongly coordinated or they would all be removed at room temperature, which is not the case. They can all be removed by evacuation at 400°C. If one evacuates at room temperature for the order of 10 h, one obtains a deuterium modulation pattern that is much less deep and that corresponds to six deuteriums at a similar distance of 0.27 nm, corresponding to three waters coordinated to Cu^{2+} as shown in Fig. 4b. So it is possible to control the number of waters coordinated to the cupric ion by thermal and evacuation treatment. One can reduce the number of coordinated waters to two or one by

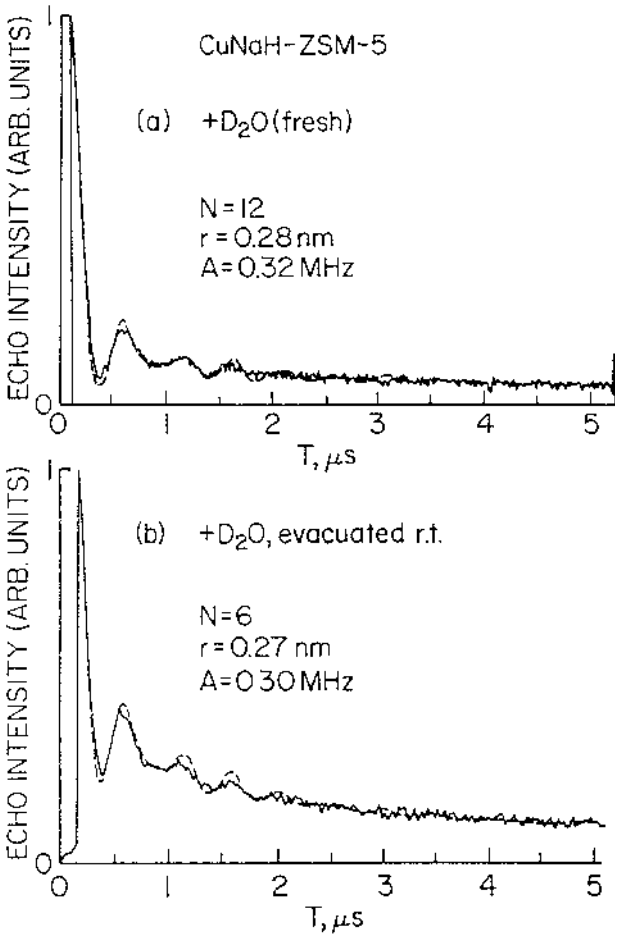

Fig. 4 Experimental (——) and simulated (----) three-pulse ESEM spectra recorded at 4 K of CuNaH-ZSM-5 (a) with adsorbed D_2O and (b) with adsorbed D_2O followed by evacuation at room temperature. (From Ref. 20.)

evacuation at 60°C or 100°C, respectively. If one evacuates at 400°C one sees no deuterium modulation, meaning that the Cu^{2+} has lost all of its coordinated waters. This is a very important example because it shows that one can actually follow the stepwise loss of multiple adsorbates coordinating to a metal ion in a zeolite or in other microporous and mesoporous materials. This is true for other adsorbates as well and is consequently important for understanding how a catalytically active metal ion is coordinated when it participates in a catalytic reaction.

C. Control of Transition Metal Ion Site

This case study involves control of the ion exchange site adopted by a paramagnetic cupric ion in zeolite X (21). Figure 5 shows the structure of zeolite X and shows typical cation ion exchange locations as roman numerals. Zeolite X has a larger alpha cage than zeolite A and has similar size beta cages. Typical exchangeable ion sites are site II which is the 6-ring between the alpha and beta cages, II' recessed into the beta cage, II* recessed into the alpha cage, and I in the

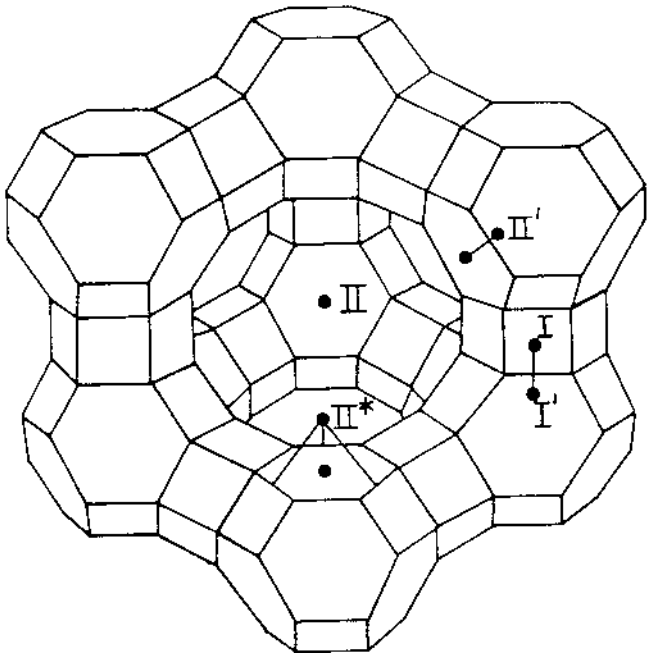

Fig. 5 Cation sites and their designations in X zeolite. (From Ref. 22.)

hexagonal prism connecting two beta cages. The point of this example is that the ion-exchange site of a small amount of cupric ion can be controlled by the major charge-compensating cation present in the zeolite.

For example, in CuNa-X zeolite in the fully hydrated state the cupric ion has no waters directly coordinated to it. This is determined by rehydrating with deuterated water and finding no deuterium modulation. This indicates that the cupric ion is in site SI in a hexagonal prism where there is no space to coordinate to water molecules. In this site, cupric ion is coordinated to six oxygens, three from the upper 6-ring of the hexagonal prism and three from the lower 6-ring of the hexagonal prism. If one heats this CuNa-X zeolite to 400°C to dehydrate the zeolite, one sees that the ESR and ESEM patterns remain the same. This supports that Cu^{2+} is not coordinated to any waters even in hydrated CuNa-X zeolite. For CuNa-X zeolite the major cocation is sodium ion, which is reasonably small so that a small amount of cupric ion exchanged into Na-X zeolite can penetrate into site SI in a hexagonal prism where it is most stable.

However, if one exchanges a small amount of cupric ion into K-X zeolite, the potassium ion is larger than sodium ion and its location in sites SII, SII*, and SII' blocks the entrance of cupric ion into a hexagonal prism SI site. So for Cu^{2+} exchange in D_2O into K-X zeolite, the Cu^{2+} shows deuterium modulation from coordinated waters. The deuterium modulation analysis shows that Cu^{2+} is coordinated to three water molecules and other information indicates that Cu^{2+} is located in the alpha cage in the SII* position. After heating to 50–100°C the cupric ion coordination reduces to two waters, and this and the *g* values indicate that Cu^{2+} is in a SII position in a 6-ring betweeen the alpha and beta cages with pentagonal bipyramidal coordination involving three oxygens of the 6-ring and two waters. With further heating to 400°C no deuterium modulation is detected indicating that complete dehydration has occured. The Cu^{2+} *g* values are then consistent with distorted octahedral coordination in site SI. Cu^{2+} has been able to move into site SI with the additional thermal energy available and squeeze past the blocking potassium ions.

These contrasting Cu^{2+} site locations in CuNa-X and CuK-X are summarized by the following equations.

$$\text{CuNa} - \text{X: Hydrated } Cu_0(\text{SI}) \xrightarrow{400^\circ\text{C}} Cu_0(\text{SI})$$

$$\text{CuK} - \text{X: Hydrated } Cu_{\text{III}}(\text{SII*}) \xrightarrow{100^\circ\text{C}} Cu_{\text{II}}(\text{SII}) \xrightarrow{400^\circ\text{C}} Cu_0(\text{SI})$$

One sees that the location in the X zeolite contrasts the location of a transition metal ion such as cupric ion. Consequently, the location can be used to control the site of a potentially catalytically active metal ion in X zeolite and other materials.

D. Observation of Reaction Intermediates

Next, we show how electron spin-echo modulation can be used to detect a catalytic reaction intermediate (22). The example here involves deuterated ethylene dimerization on PdCa-X zeolite where some Pd^{2+} is reduced to paramagnetic Pd^{+}, which is the active site. The major cocation, Ca^{2+}, controls the location of Pd^{+} to sites SII and SII*, where it can coordinate with ethylene and effect ethylene dimerization. Figure 6 shows the inset ESR spectra after reaction is initiated and one can see that there are several Pd^{+} species present as indicated by three resolved $g_{\|}$ features. Feature B corresponds to an isolated Pd^{+} ion. Feature C, for which the electron spin-echo modulation is shown together with a simulation and the simulation parameters, indicates that the Pd^{+} is coordinated to one molecule of deuterated ethylene. This seems consistent with p-bond interaction since there are four equivalent deuteriums interacting with Pd^{+} at 0.40 nm. This is a typical coordination p-bond coordination distance for second-row transition metal ions. This is the first reaction intermediate of Pd^{+} interacting with ethylene.

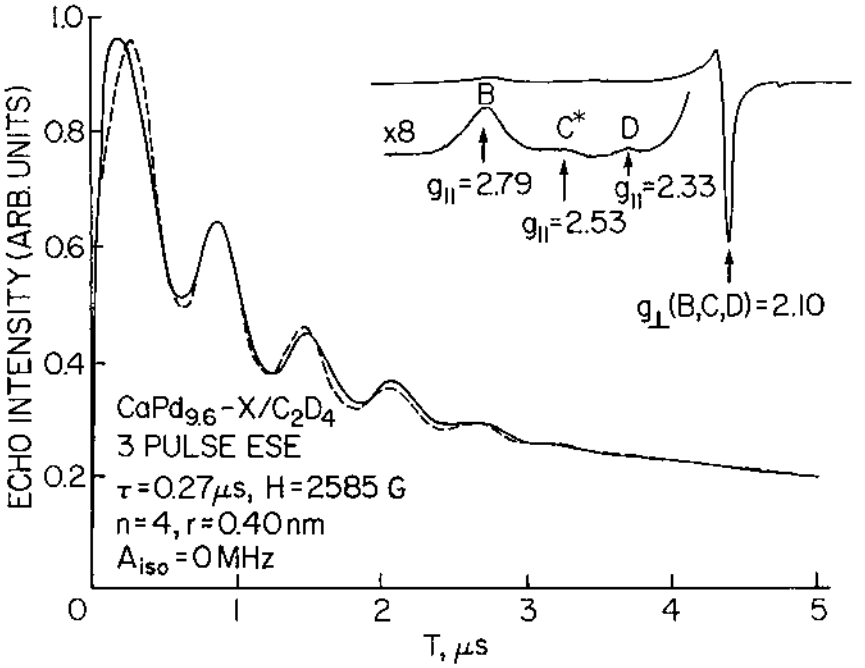

Fig. 6 Experimental (——) and simulated (----) three-pulse ESEM spectra at 4 K of $NaPd_{12.5}$-X with adsorbed C_2D_4 at 50°C at $g_{\|} = 2.53$ indicated by an asterisk inset ESR spectrum at 77 K. (From Ref. 22.)

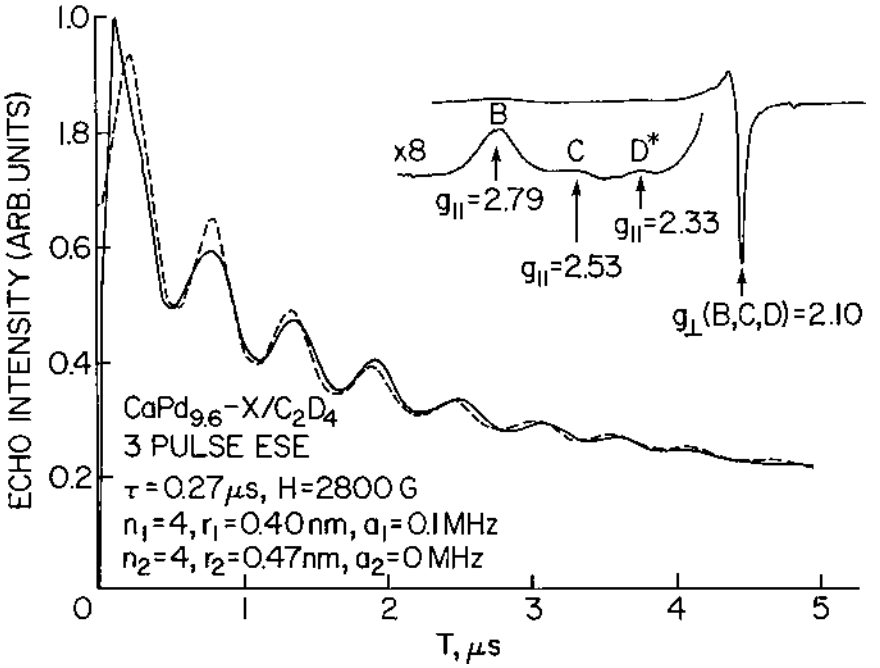

Fig. 7 Experimental (——) and simulated (----) three-pulse ESEM spectra at 4 K of $CaPd_{9.6}$-X with adsorbed C_2D_4 at $g_{\|} = 2.33$ as indicated by an asterisk on the inset ESR spectrum at 77 K. (From Ref. 22.)

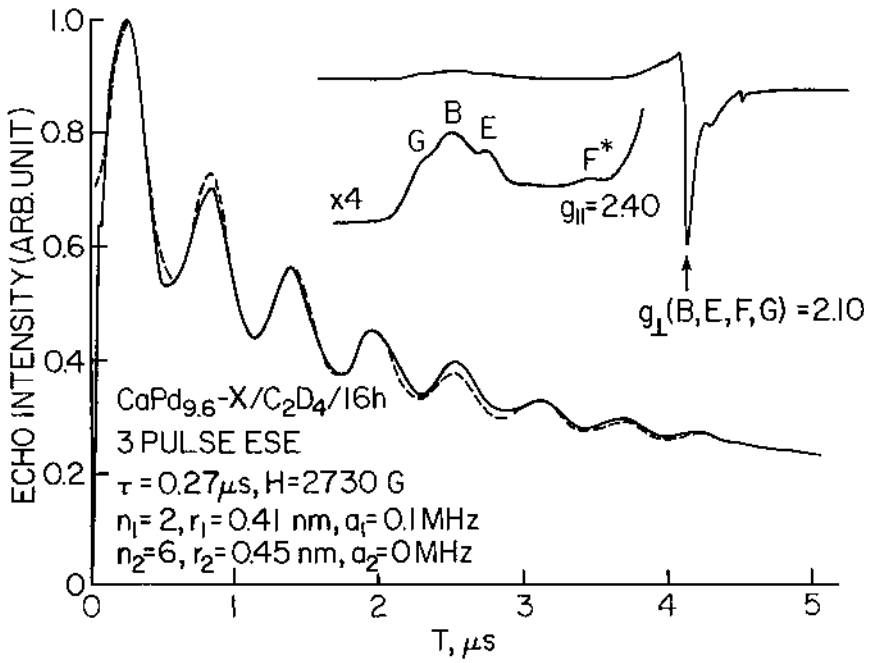

Fig. 8 Experimental (——) and simulated (----) three-pulse ESEM spectra at 4 K of $CaPd_{9.6}$-X with adsorbed C_2D_4 at $g_{\|} = 2.40$ as indicated by an asterisk on the inset ESR spectrum at 77 K. (From Ref. 22.)

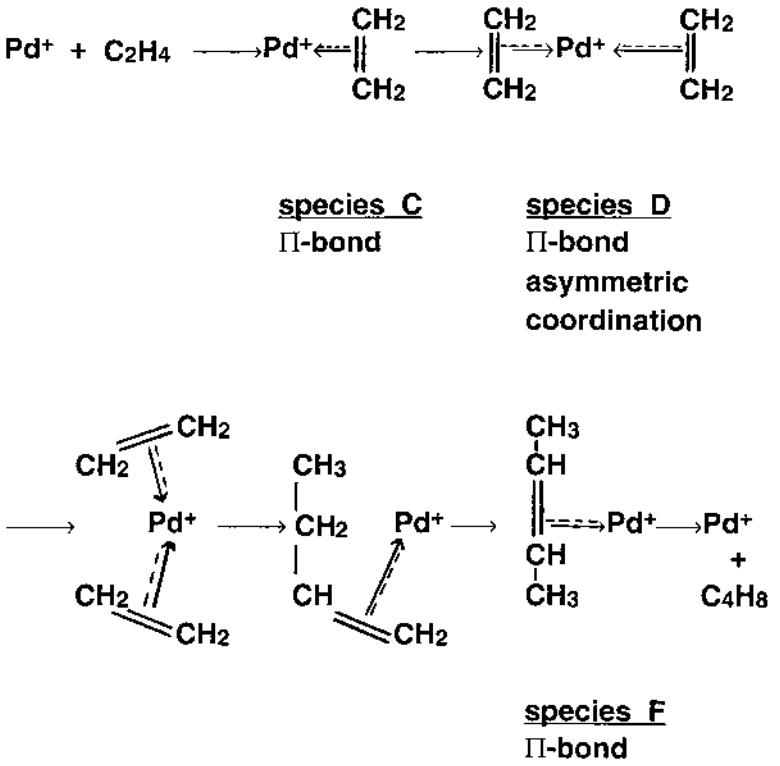

Fig. 9 Pd^+-catalyzed ethylene dimerization mechanism on PdCa-X zeolite.

It should be noted that the use of Ca-X zeolite is critical here because the calcium ion controls the location of the Pd^+ ion to be in site SII or SII* where it can coordinate with ethylene. Thus, the information shown in the section on control of metal ion site has been used for this study of a catalytic reaction. If one uses Na-X zeolite, the ion-exchanged Pd^{2+} locates into the beta cage or into the hexagonal prism, and Pd^+ formed after activation cannot coordinate with ethylene and consequently does not cause ethylene dimerization.

Figure 7 shows the deuterium modulation associated with Pd^+ at site D. This modulation is somewhat deeper and corresponds to Pd^+ interacting with two ethylene molecules at a later stage in the reaction mechanism. Furthermore, the two molecules seem to be at somewhat different distances indicated by two sets of parameters, four deuteriums coordinated at 0.40 nm (one ethylene) and four more deuteriums interacting at 0.47 nm (second ethylene). This asymmetry may possibly facilitate the final rearrangement of the two coordinated ethylenes to the final butene product.

After the reaction has proceeded until product butene is observed by gas chromatography in a flow system, the PdCa-X sample is quenched to 77 K and ESR shows a new $g_{\|}$ feature F in Fig. 8. The deuterium modulation is analyzed to show two deuteriums at 0.41 nm and six deuteriums at 0.45 nm, which is consistent with Pd^+ coordinated with the butene product as shown in Fig. 9. Figure 9 summarizes the ethylene dimerization reaction mechanism showing the three intermediate species that have been detected by deuterium electron spin-echo modulation. First, species C shows the initial interaction of one molecule of ethylene with Pd^+. Then species D shows the interaction of a second ethylene coordinated directly with

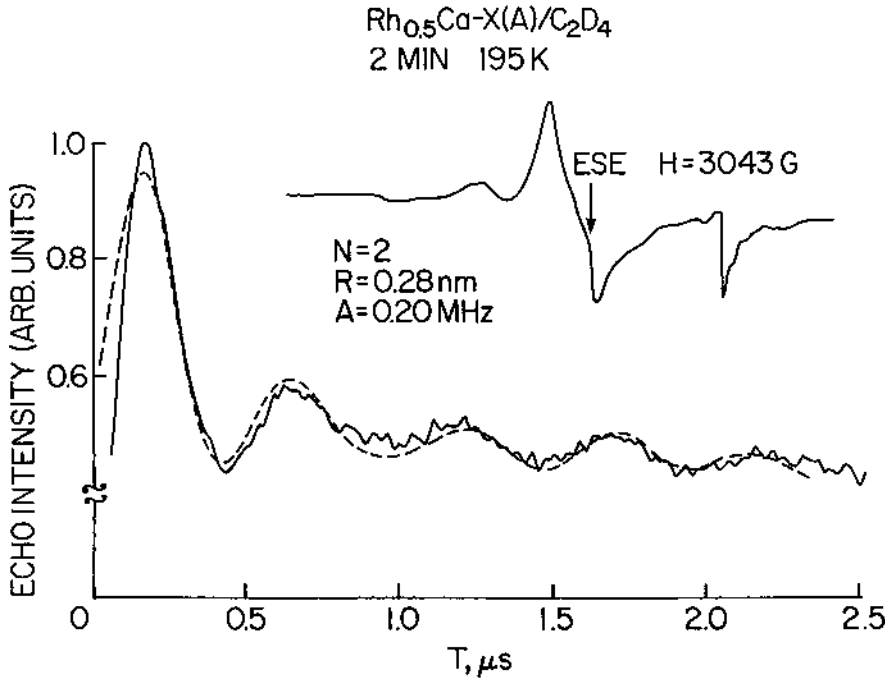

Fig. 10 Three-pulse ESEM spectrum with corresponding ESR spectrum of $Rh_{0.5}Ca$-X (A) followed by C_2D_4 adsorption at 77 K and warming to 195 K for 2 min. The ESEM was measured at H = 3043 G with τ = 0.30 μs. The dashed trace is a calculated spectrum, and the corresponding best-fit parameters are shown. (From Ref. 23.)

Pd^+ with asymmetrical coordination relative to the first coordinated ethylene. This structure D rules out the possibility that Pd^+ distorts the electronic distribution of the first coordinated ethylene so that a second ethylene coordinates to the first ethylene. Then, a rearrangement of the two ethylenes occurs for which we do not see a separate isolated intermediate. Finally, the butene product forms which is seen as intermediate species F where the Pd^+ is coordinated to a molecule of butene. The butene then desorbs and the catalytic reaction continues the cycle.

Ethylene can also be dimerized by Rh^{2+} but the mechanism is quite different (23). Figure 10 shows an ESR spectrum of Rh^{2+} and deuterium electron spin-echo modulation for RhCa-X zeolite with adsorbed ethylene. In this case, the ESEM spectrum of the intermediate gives much different parameters for ethylene coordination, with only two deuteriums interacting at a very close distance of 0.28 nm. This indicates that the Rh^{2+} has not a π-bond interaction with the ethylene but a σ-bond interaction with only one end of the ethylene, so that two ethylene deuteriums are closer to Rh^{2+} than the other two. Thus, the ethylene dimerization mechanism is quite different for Rh^{2+} vs. Pd^+. Furthermore, the coordination of ethylene to Rh^{3+} originally in RhCa-X seems to be reductive to produce Rh^{2+}, which is paramagnetic and actually coordinates to one ethylene as observed. As shown in Fig. 11, it is possible that Rh^+ is formed by reductive addition when a second ethylene coordinates to the Rh^+–ethylene complex and that an Rh^+ complex is the active valence state for the actual dimerization.

Overall one can see that if one is fortunate enough to isolate one or more paramagnetic reaction intermediates, ESEM can determine the geometry of the stepwise intermediates in a

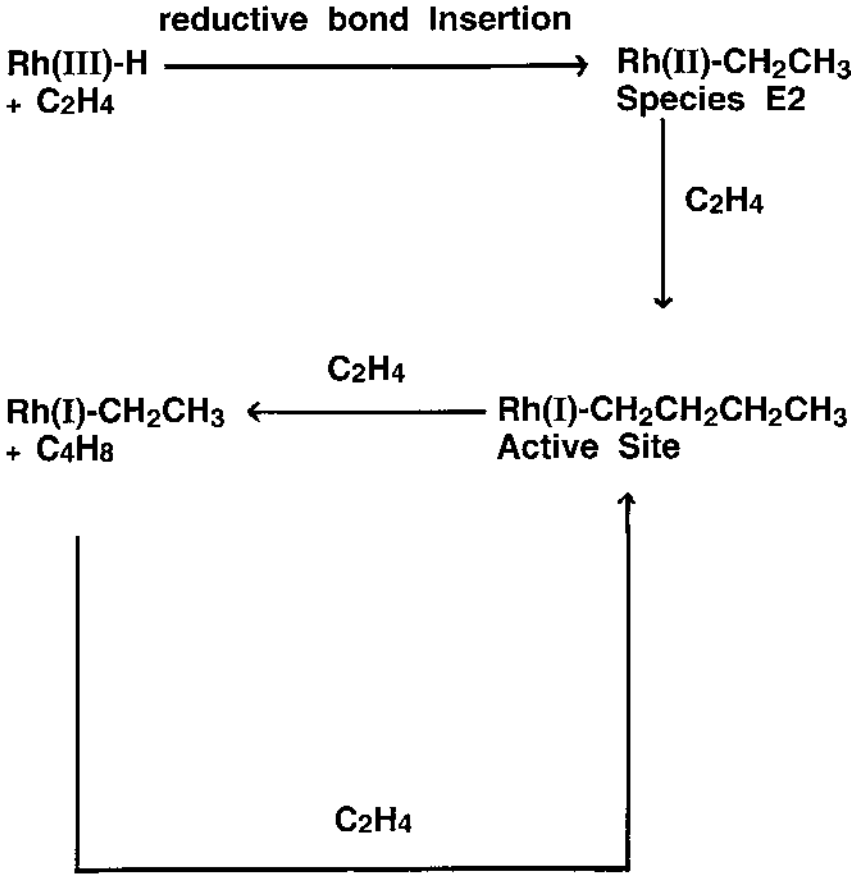

Fig. 11 Rh^{2+}-catalyzed ethylene dimerization mechanism on RhCa-X zeolite.

catalytic reaction to a degree that is seldom accomplished by other techniques. Of course, other spectroscopic and scattering techniques are also advantageously used to study such isolated reaction intermediates.

E. Cupric Ion Movement During Dehydration

This case study involves the use of electron spin-echo modulation to follow changes in the location of cupric ion during dehydration in microporous silicoaluminophosphate-18 (SAPO-18) by analyses of ^{31}P modulation (24). Figure 12 shows the framework structures of SAPO-18 and a view of the largest pear-shaped cavity, which is located between eight hexagonal prisms. Figure 13 shows the three-pulse ^{31}P modulation associated with cupric ion exchanged into SAPO-18 for completely hydrated and completely dehydrated Cu-SAPO-18. It can been seen that the modulation is deeper in dehydrated Cu-SAPO-18, indicating that Cu^{2+} has moved closer to the phosphorus nuclei during the dehydration process. The simulation parameters for the ^{31}P modulation show that the Cu^{2+}-P distance decreases from 0.44 nm in the hydrated material to 0.32 nm in the dehydrated material. When the dehydrated material is rehydrated the copper moves back close, but not quite to, its "original" position at 0.42 nm for the Cu^{2+}-P distance.

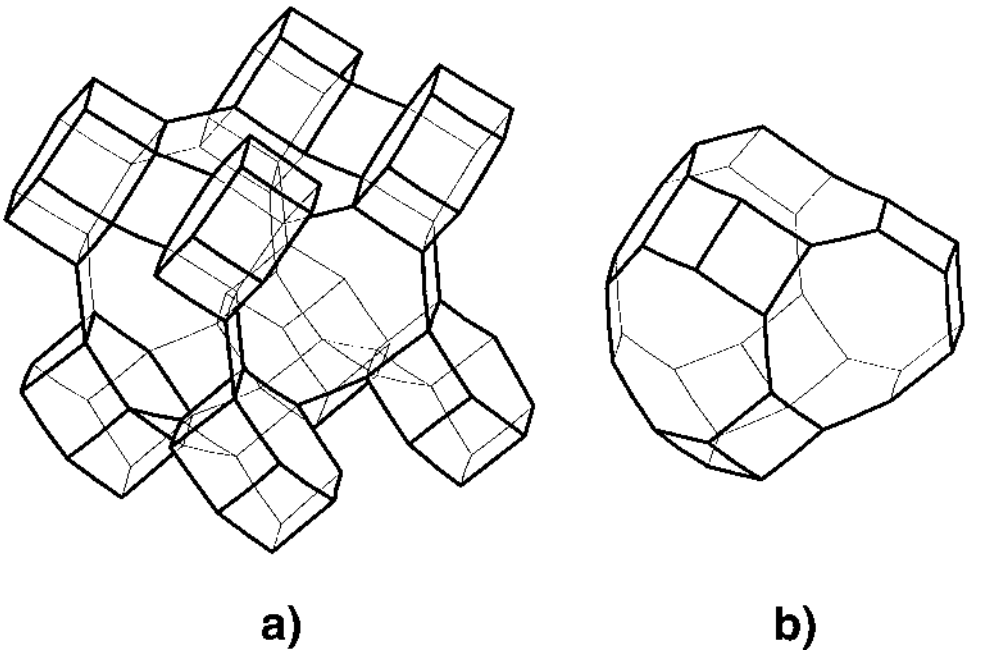

Fig. 12 SAPO-18 structure (AEI type): (a) hexagonal prisms surrounding the pear-shaped supercage, and (b) the pear-shaped supercage. (From Ref. 24.)

Based on Cu^{2+} locations in other SAPO-*n* materials, the most probable location for Cu^{2+} in SAPO-18 is on a line perpendicular to a hexagonal prism displaced into the large, pear-shaped cavity. In that location Cu^{2+} can be fully hydrated by six water molecules, which is independently verified by analysis of deuterium modulation. Then, as dehydration proceeds one can envision that the cupric ion moves toward the 6-ring plane at the end of the pear-shaped cavity and interacts more strongly with the three phosphorus atoms of the 6-ring. Actually somewhat fewer than three phosphorus atoms interact because silicon substitutes for some phosphorus. Analyses show an average of 2.7 phosphorus atoms for a 6-ring plane interacting with the cupric ion. So from the known structure of SAPO-18, one can calculate the distance of cupric ion from the plane of the 6-ring window by the plot shown in Fig. 14. The ^{31}P modulation parameters fit a distance of 0.36 nm from the 6-ring for Cu^{2+} displaced into the pear-shaped cavity for hydrated Cu-SAPO-18. As dehydration occurs the cupric ion moves to site I, which is 0.17 nm displaced from the 6-ring into the pear-shaped cavity. So the cupric ion moves a remarkable 0.19 nm or 1.9 Å in the process of dehydration. Furthermore, when dehydrated Cu-SAPO-18 is rehydrated, the cupric ion moves back further into the pear-shaped cavity, to 0.33 nm from the 6-ring which is almost, but not quite, back to its original position in initially hydrated Cu-SAPO-18. This is shown schematically in Fig. 15.

By using deuterated water one can analyze the deuterium modulation to determine the hydration structure of the cupric ion in fully hydrated Cu-SAPO-18. Cu^{2+} is found to be coordinated to six water molecules in a distorted octahedral configuration as expected. In the dehydrated state no interaction with deuterium from deuterated water is observed by deuterium modulation. This verifies that the cupric ion has been completely dehydrated and is predominantly intereacting with three oxygens, which are puckered upward in a 6-ring at the end of the pear-shaped cavity in SAPO-18. This is an excellent example of how analyses of the appropriate

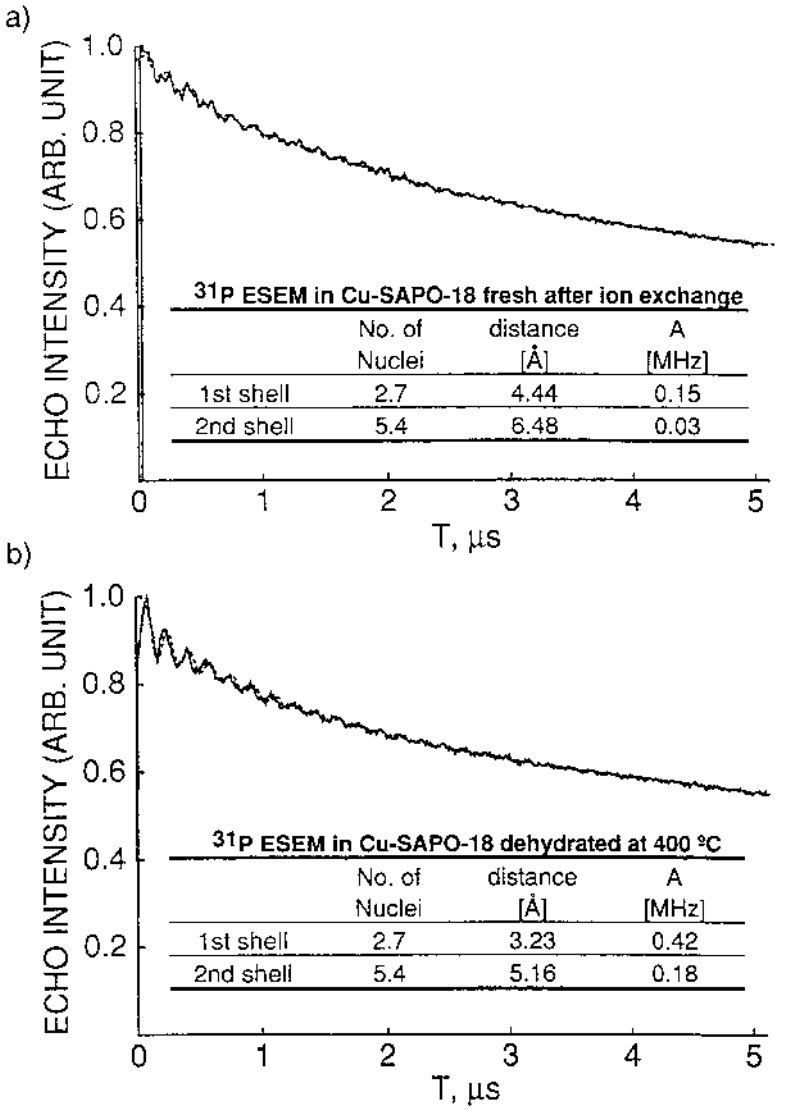

Fig. 13 Three-pulse ^{31}P ESEM at 5 K (solid line) and simulation (dashed line) for (a) fresh Cu-SAPO-18 after ion exchange and (b) Cu-SAPO-18 dehydrated at 400°C overnight. (From Ref. 24.)

nuclear modulation cannot only locate a paramagnetic metal ion within a microporous oxide structure but can also show quantitatively where and how much it moves during a process of dehydration or of general desolvation.

F. Distinguishability of Two Metal Ion Sites

Another example of the use of ^{31}P modulation to assign different metal ion locations in SAPO materials is shown by the determination of two different ion-exchange locations of Pd^{+} in SAPO-11 (25). Figure 16 shows the ESR spectra of Pd^{+} in SAPO-11 where paramagnetic Pd^{+} has been produced by thermal activation in which water reduces Pd^{2+} to Pd^{+}. The two $g_{\|}$ values

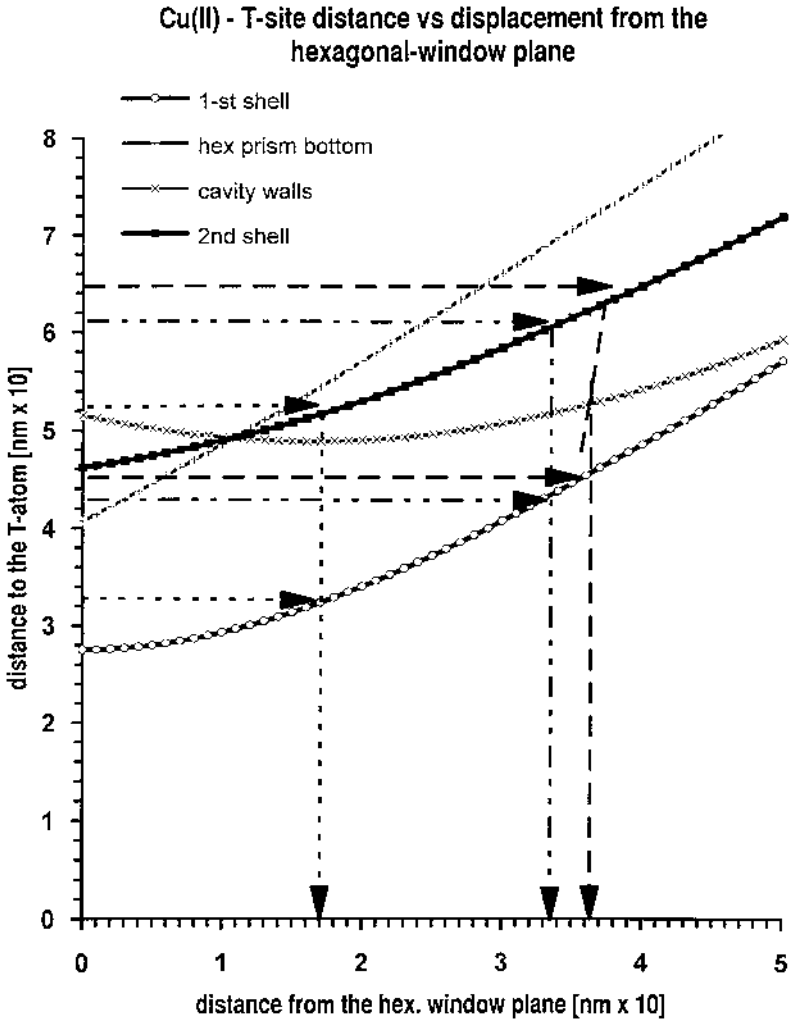

Fig. 14 Displacement of Cu^{2+} ion from the plane of the hexagonal ring in the supercage of Cu-SAPO-18 from three pulse ^{31}P ESEM simulations. The second shell curve (solid squares) is an average of the curves for the distances to the bottom of the hexagonal prism (+) and the distances to T sites located on the wall of the cavity (x). (From Ref. 24.)

show that there are two different Pd^{+} sites designated A and B. By treating these with oxygen, it is seen that the ESR intensity of Pd^{+} in site B decreases to a greater extent and hence site B is more accessible to a reactive adsorbate like oxygen than is Pd^{+} in site A. Figure 17 shows the experimental and simulated ^{31}P modulation for Pd^{+} in SAPO-11 where the magnetic field position has been selected for site A at $g_{\|}$ = 2.9. The ^{31}P modulation corresponds to five phosphorus nuclei interacting at 0.38 nm. The presence of five phosphorus nuclei suggests that this Pd(I) is located in a site where it interacts with two 6-rings (there are an average of about 2.5 phosphorus per 6-ring since some of the phosphorus is replaced by silicon in SAPO-11). This is consistent with site I in Fig. 18. In contrast, the lower section of Fig. 17 shows weaker phosphorus modulation for Pd^{+} at site B at $g_{\|}$ = 2.6. The simulation parameters correspond to 2.5 ^{31}P

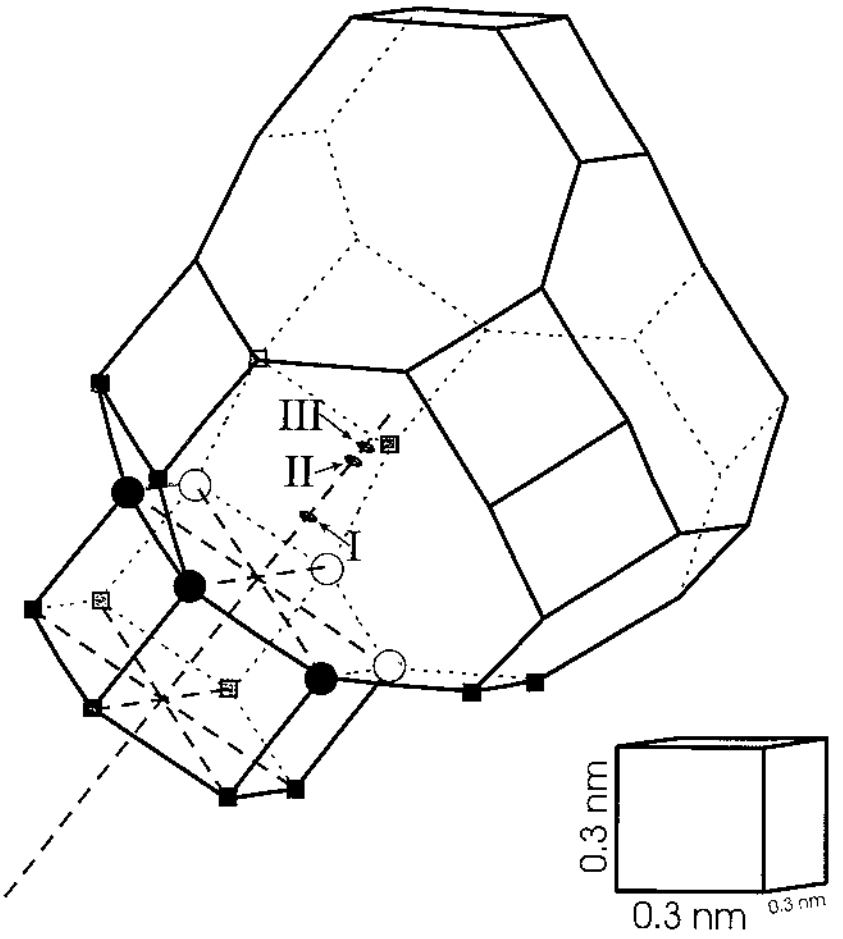

Fig. 15 Schematic of first (circles) and second (squares) shell T-site positions around Cu^{2+} in Cu-SAPO-18 from three-pulse ^{31}P ESEM data and the Cu^{2+} positions in (I) Cu-SAPO-18 dehydrated at 400°C overnight, (II) Cu-SAPO-18 rehydrated at 100°C overnight, and (III) fresh Cu-SAPO-18 after ion exchange. (From Ref. 24.)

at a distance of 0.36 nm. Interaction with only 2.5 phosphorus nuclei indicates interaction of Pd^{+} species B with only one 6-ring, which is consistent with site II* projected into the large channel in Fig. 18. These two site assignments are also consistent with Pd^{+} species B being in a more exposed site as shown by the effect of oxygen. As shown in Fig. 18, site SII* is much more exposed to an adsorbate like oxygen than is site I in a hexagonal prism. Thus, these analyses have been able to distinguish between two different locations of paramagnetic Pd^{+} when produced in SAPO-11 microporous oxide.

G. Distinguishability of Metal Ions in Oxide Framework vs. Nonframework Sites

In comparison with the determination of paramagnetic ion locations in ion-exchange sites in microporous oxide materials, a contrasting example where a paramagnetic ion is located in a

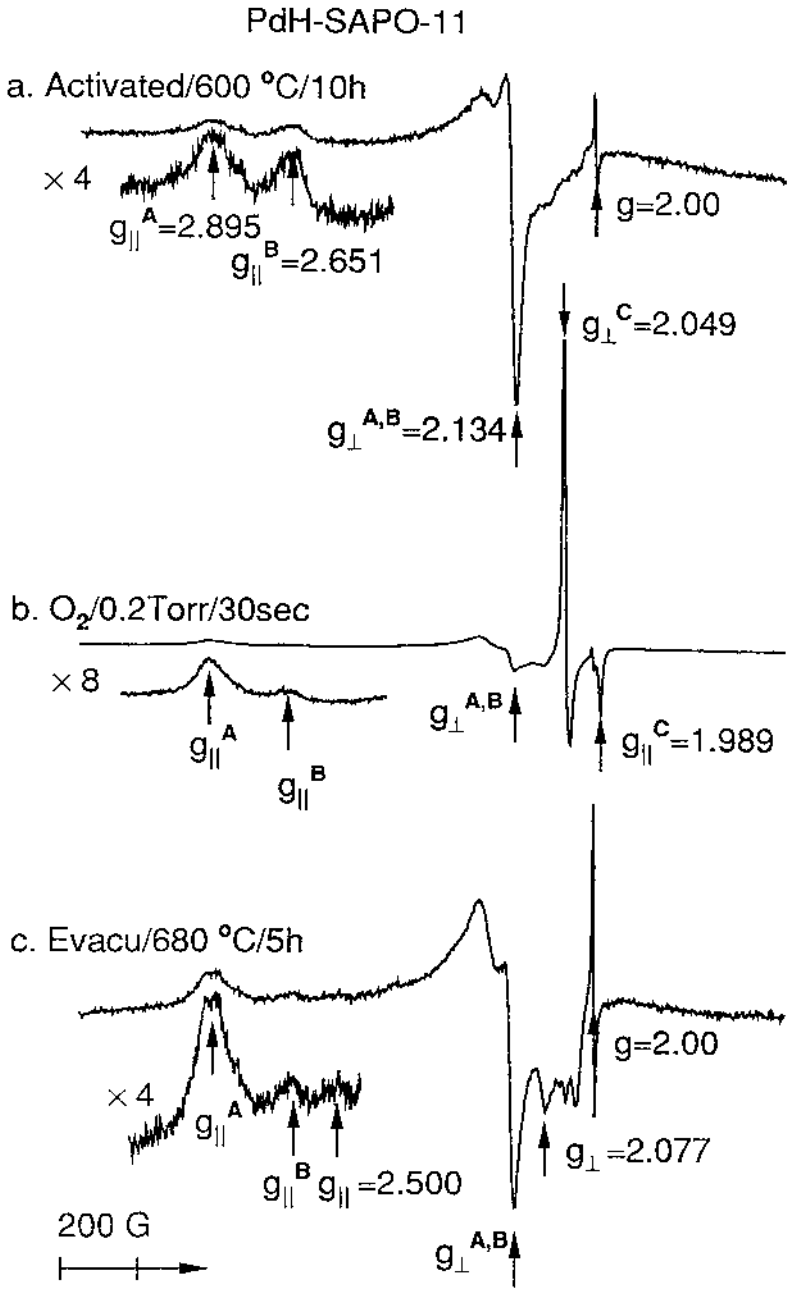

Fig. 16 ESR spectra at 77 K of (a) PdH-SAPO-11 activated at 600°C (b) after subsequent adsorption of 0.5 Torr of oxygen at room temperature for 5 min or (c) after further heating at 600°C for 5 h. (From Ref. 25.)

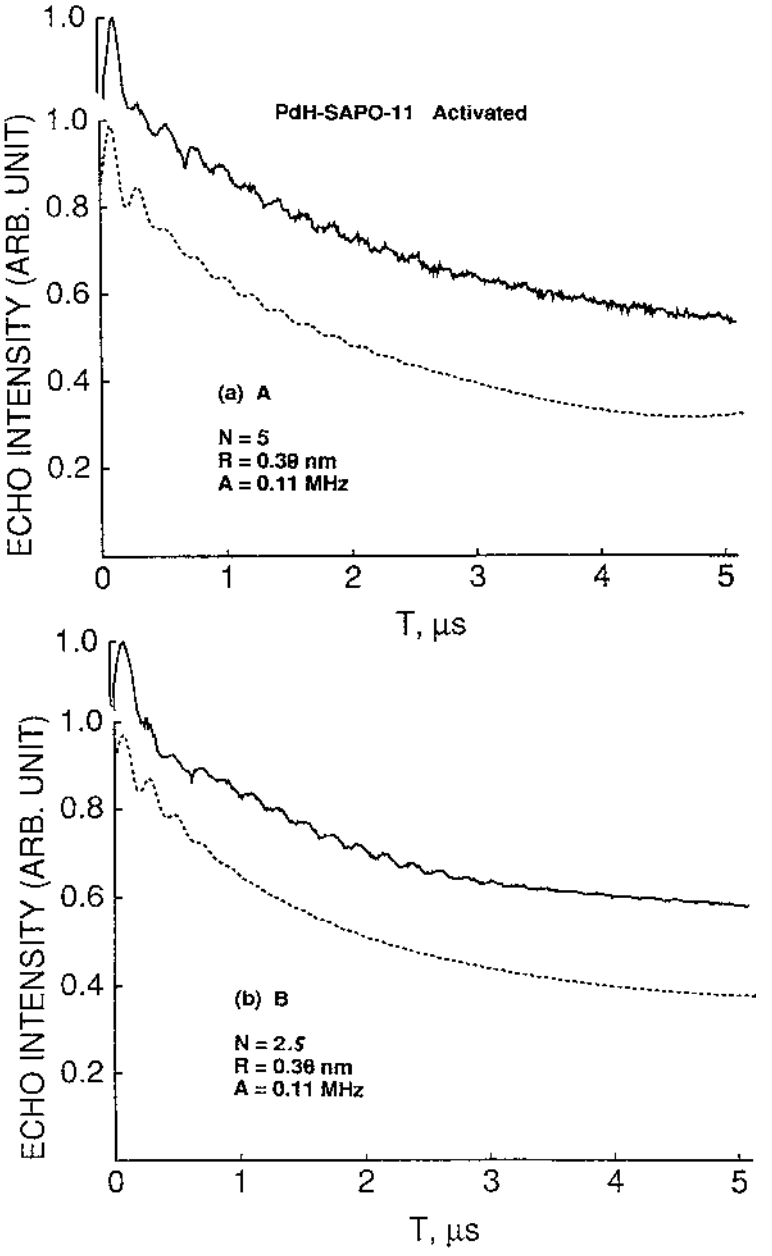

Fig. 17 Experimental (——) and simulated (----) three-pulse ESEM spectra at 4 K of activated PdH-SAPO-11 at the magnetic field corresponding to (a) the $g_{\|}$ value of Pd^{+} species A and (b) the $g_{\|}$ value of Pd^{+} species B showing ^{31}P modulation. (From Ref. 25.)

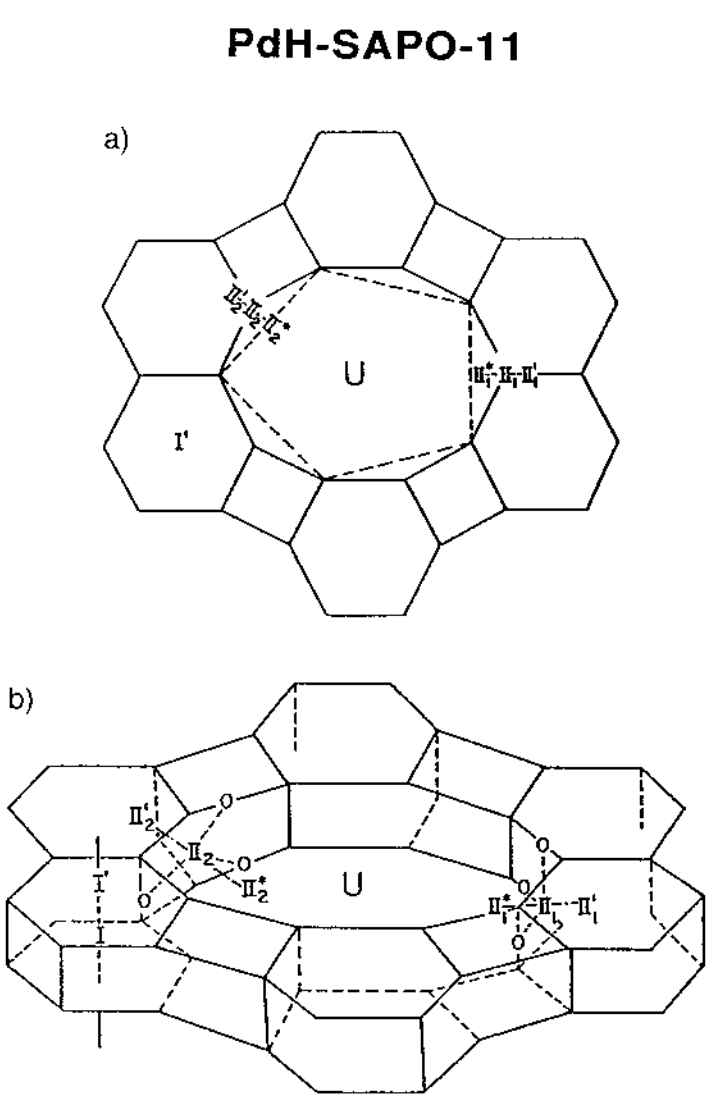

Fig. 18 (a) View along the elliptical 10-ring channel axis of SAPO-11 where the dashed lines show the edges of six-ring windows that form the surfaces of a 10-ring channel. (b) A simplified structure of SAPO-11 showing possible cation positions. (From Ref. 25.)

framework site is now shown (26). Clear-cut framework siting is difficult to determine by physical techniques in general. But ESEM seems to play a role in locating whether a paramagnetic metal ion is in a framework site with tetrahedral coordination to oxygen like other tetrahedral (T) atoms in contrast to an ion-exchange site. A key comparison to make is to carry out experiments on synthesized material where the metal ion *may* be in a framework site and on ion-exchanged material where the metal ion is clearly not in a framework site.

The example here involves Ni^{2+} in SAPO-5. SAPO-5 has a structure related to that of SAPO-11 shown in Fig. 19. SAPO-5 has a larger 12-ring channel compared with a 10-ring channel in SAPO-11. Since SAPO-5 has some ion-exchange capacity, Ni^{2+} can be introduced

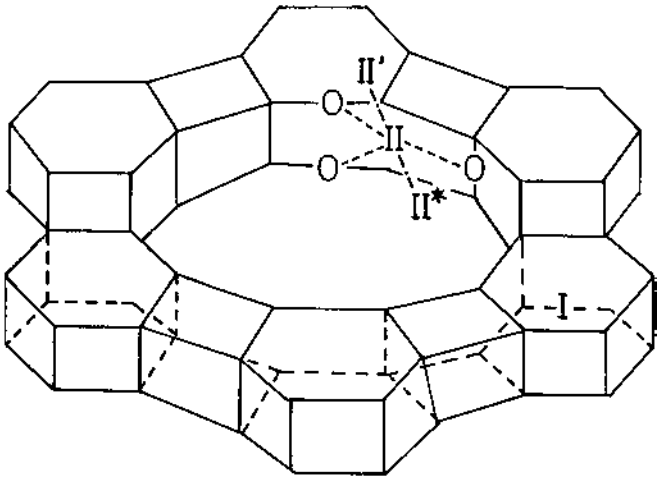

Fig. 19 SAPO-5 structure showing possible cation positions.

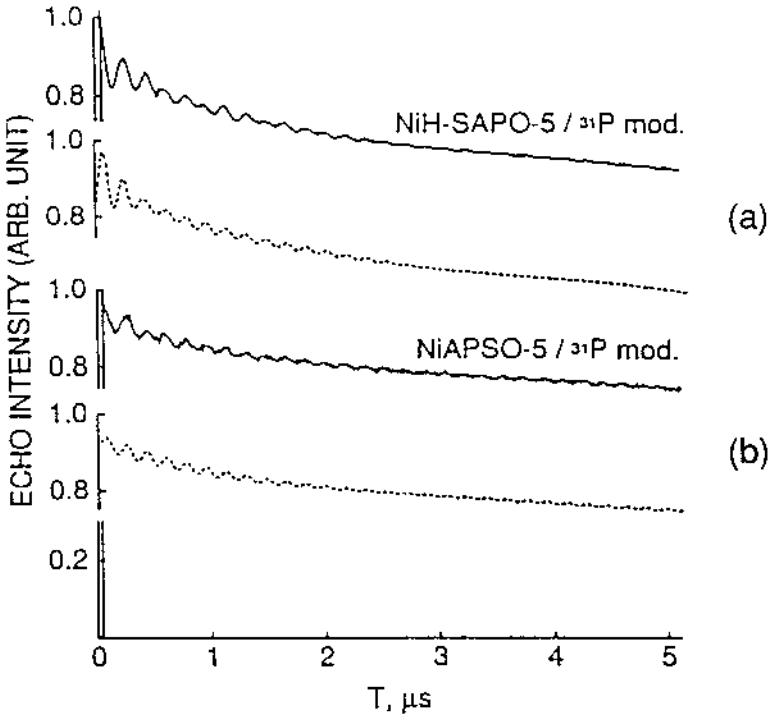

Fig. 20 Experimental (——) and simulated (----) three-pulse ESEM spectra showing ^{31}P modulation for (a) NiH-SAPO-5 and (b) NiAPSO-5 after hydrogen reduction and subsequent 10-min evacuation at room temperature. Spectra recorded at 4 K with $\tau = 0.27$ μs to suppress ^{27}Al modulation. (From Ref. 26.)

by ion exchange. Also it can be introduced by direct synthesis by including a nickel salt in the synthesis gel. At low concentration of nickel ion, it may be incorporated into a framework site substituted for an aluminum or phosphorus. Some Ni^{2+} is reduced to paramagnetic Ni^{+} by thermal or hydrogen reduction. Figure 20 shows the ^{31}P modulation of paramagnetic Ni^{+} in ion-exchanged NiH-SAPO-5 and in synthesized NiAPSO-5 where the hyphen after the metal ion symbol indicates ion-exchanged material. The simulation parameters are somewhat different. The parameters for the ion-exchanged material NiH-SAPO-5, where the Ni^{+} is produced by reduction with gaseous hydrogen, are 5.2 phosphorus nuclei at 0.33 nm, which is consistent with ion exchange in site I as just discussed for the case of Pd^{+}in SAPO-11. In contrast, the parameters for Ni^{+} in synthesized NiAPSO-5 correspond to 8.8 phosphorus nuclei at 0.51 nm, which is consistent with Ni^{+} in a framework site substituting for phosphorus. If Ni^{+} substituted for a framework aluminum site, the ^{31}P modulation would be much deeper corresponding to a Pd^{+} to ^{31}P distance of about 0.31 nm.

To confirm this difference between framework and ion-exchange sites, adsorbate geometry has been determined for both ion-exchanged NiH-SAPO-5 and synthesized NiAPSO-5 with both methanol and ethylene. Figure 21 a and b shows the absorbate geometries deduced by deuterium modulation from specifically deuterated methanol, namely, separately deuterated in the methyl group and at the hydroxyl proton position. Analyses of ion-exchanged NiH-SAPO-5 give rise to two directly coordinated methanols with distances from Ni^{+} to the average deuterium positions in the methyl group of 0.34 nm and 0.29 nm to the deuterium in

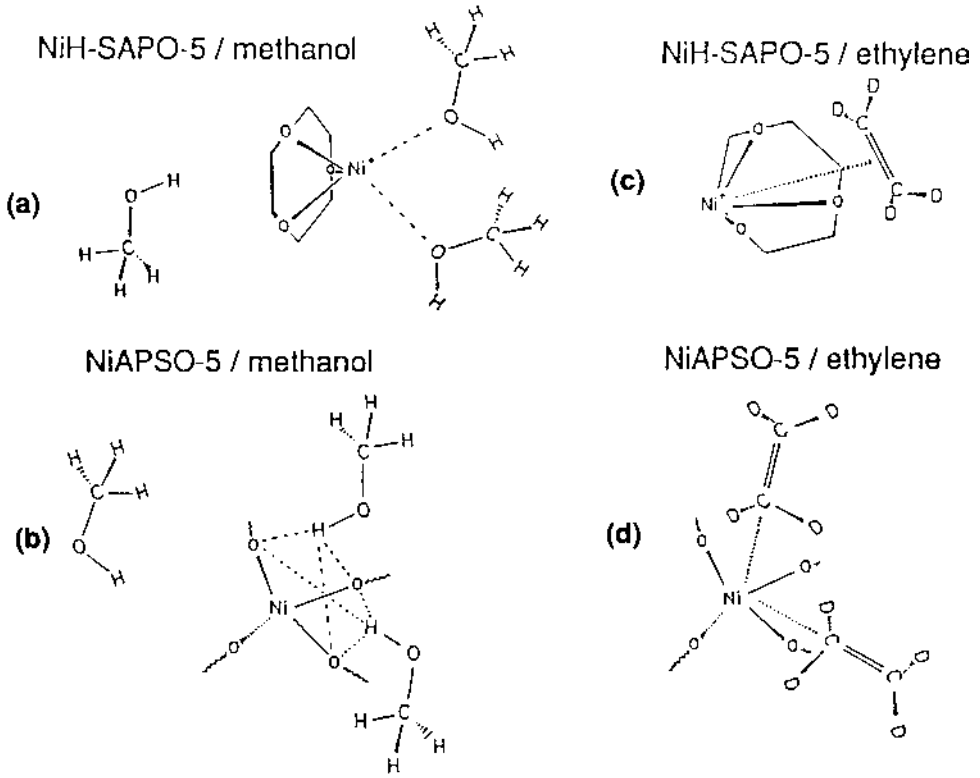

Fig. 21 Schematic diagram of Ni^{+}coordinated to methanol in (a) NiH-SAPO-5 and (b) NiAPSO-5 and to ethylene in (c) NiH-SAPO-5 and (d) NiAPSO-5. (From Ref. 26.)

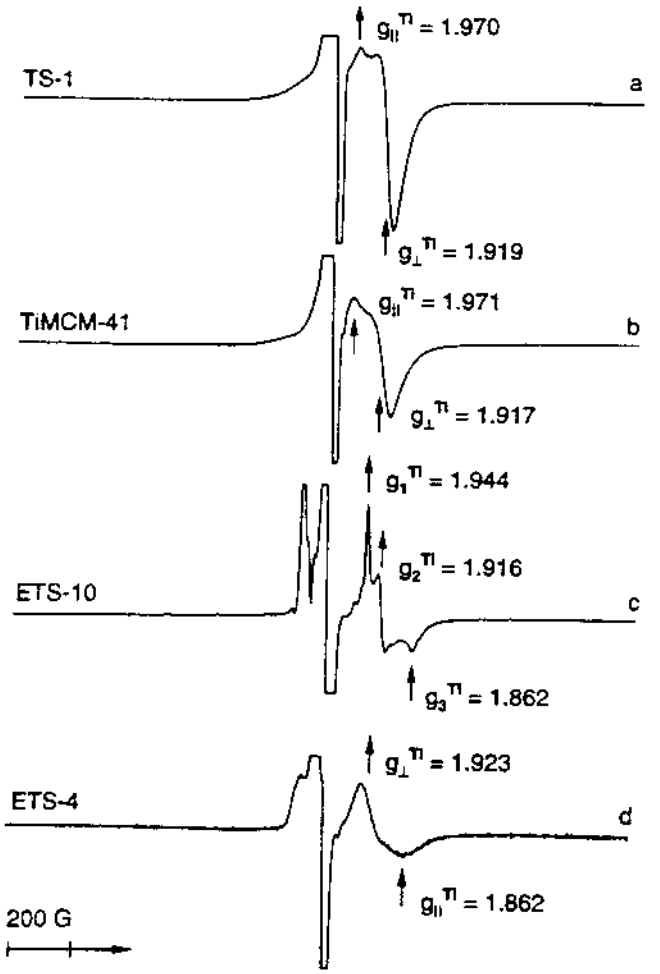

Fig. 22 ESR spectra at 77 K of (a) TS-1, (b) TiMCM-41, (c) ETS-10, and (d) ETS-4 after γ irradiation at 77 K of activated samples. (From Ref. 28.)

the hydroxyl group. Together with the known geometry of methanol, the adsorbate geometry for NiH-SAPO-5 is as shown in Fig. 21a, with the dipole of the methanol molecule oriented toward the cationic Ni^+ species. This geometry has been typically found for solvation of metal ions by methanol in a variety of microporous materials.

In contrast, the geometry of adsorbate methanol molecules around the Ni^+ in synthesized NiAPSO-5 material is quite different since there is a short Ni^+-D distance of 0.25 nm to the hydroxyl deuterium indicating that the OH or OD bond of the methanol is oriented toward the Ni^+. This bond orientation is what one expects from a locally negative site. This is the way that methanol solvates a localized electron in glassy methanol (27). This orientation seems rational if the Ni^{2+} that is converted to Ni^+ has in fact substituted for a P^{5+} species in the framework since this site will be locally negative and this local charge will control the geometry of the methanol orientation around Ni^+ in a framework site. So the difference in methanol adsorbate geometry between ion-exchanged NiH-SAPO-5 and synthesized NiAPSO-5 is consistent with different Ni^+ sites. The detailed analyses of the geometry determined by the deuterium modulation of

adsorbate methanol is totally consistent with the Ni^+ in NiAPSO-5 being in a framework phosphorus site and with Ni^+ in NiH-SAPO-5 being in an exposed ion-exchange site.

Finally, Fig. 21c and d shows the geometry determined for ethylene adsorbate interacting with Ni^+ in ion-exchanged NiH-SAPO-5 and in synthesized NiAPSO-5. In the ion-exchanged NiH-SAPO-5 material one molecule of ethylene interacts with the Ni^+ with four equivalent deuteriums from one molecule of ethylene at an Ni^+ to *D* distance of 0.35 nm. This is a typical distance found for π-bonded ethylene interaction with ion-exchanged first-row transition metal ions in microporous materials. In contrast, the Ni^+ in synthesized NiAPSO-5 shows a quite different geometry. It shows that the Ni^+ interacts with deuteriums at two different distances. One is 0.31 nm and the other is 0.55 nm. This can only be rationalized in terms of non-π-bonded interaction of the ethylene as shown in Fig. 21d, with Ni^+ in a framework site. Ni^+ in a framework site in NiAPSO-5 is sufficiently crowded by its environment so that a π-bonded interaction with ethylene is energetically unfavorable. Instead, the Ni^+ interacts with a σ-type bonding interaction to give the geometry shown in Fig. 21d. This kind of geometry has been found before for Rh^{2+} in X zeolite interacting with ethylene. So this geometry is not unprecedented.

The differences in the ESR spectra are very small for Ni^+ complexes with adsorbates between synthesized NiAPSO-5 vs. ion-exchanged NiH-SAPO-5. So one cannot say from the ESR spectrum alone that these different materials correspond to Ni^+ at different sites. But ^{31}P ESEM modulation clearly shows that there are different site positions for Ni^+ in synthesized NiAPSO-5 vs. ion-exchanged NiH-SAPO-5. Furthermore, the ^{31}P simulation parameters support framework substitution of Ni^+ for phosphorus in NiAPSO-5. Finally, analyses of deuterium modulation for the methanol and ethylene adsorbates confirm different adsorbate geometries for Ni^+ in NiAPSO-5 vs. NiH-SAPO-5. These different geometries are consistent with Ni^+framework substitution in NiAPSO-5.

H. Application of *g* Anisotropy to Determine Coordination Geometry

The anisotropy of *g* values of a paramagnetic metal ion is related to the symmetry of the electrostatic field surrounding the metal ion, which reflects its local coordination to adjacent atoms. For idealized coordination geometries the *g* anisotropy can distinguish and identify the coordination geometry. However, when distortion of the idealized geometry occurs, as is common in oxide materials, the interpretation of the *g* anisotropy may be ambiguous.

However, for Ti(III) in microporous and mesoporous oxide materials the *g* anisotropy has been successfully analyzed to distinguish between tetrahedral and octahedral coordination. This has been made possible by the existence of well-characterized titanosilicates with both tetrahedral (TS-1) and octahedral (ETS-10 and ETS-4) oxide coordinations (28).

Both hydrated and activated samples of various titanosilicates do not show any ESR signal for Ti(III) ions so the titanium exists as Ti(IV). Isolated Ti(III) ions, however, can be generated in all titanosilicates by γ-ray irradiation at 77 K of activated samples. Figure 22 shows ESR spectra at 77 K after γ-ray irradiation of several activated titanosilicate samples. The observed spectra are characterized by signals from radiation-induced hole centers known as V centers and from Ti(III) centers. The ESR spectra of TS-1 and TiMCM-41, a mesoporous silica, show a strong orthorhombic signal at $g = 2$ from V centers and an axial signal with $g_{\|} = 1.970$ and $g_{\perp} = 1.919$ from Ti(III) ions. The Ti(III) ions observed in ETS-10 and ETS-4 are different from those of TS-1 or TiMCM-41. A rhombic signal with $g_1 = 1.944$, $g_2 = 1.916$, and $g_3 = 1.891$ in ETS-10 and an axial signal with $g_{\perp} = 1.923$ and $g_{\|} = 1.862$ in ETS-4 are observed for the Ti(III) ions. The assignment of Ti(III) in various titanosilicates is based on two observations. Ti(III) centers in several titanium-containing compounds are reported to have

ESR in the same region. For example, in alkali titanates, more than one Ti(III) center is observed after γ irradiation. A broad signal with $g_\perp = 1.975$ and $g_\parallel = 1.890$ and a sharp signal with $g_\perp = 1.990$ and $g_\parallel = 1.981$ occur. They are identified as Ti(III) centers formed in TiO_6 units having one and two nonbridging oxygens, respectively (29). Also, when silicalite-1 or SiMCM-41 without Ti(IV) is γ-irradiated under the same conditions, only a signal due to V centers as in TS-1 or TiMCM-41 is observed.

The observed g components of the Ti(III) ion in various titanosilicates can be correlated to the specific crystalline field experienced by this ion. If titanium in TS-1 and TiMCM-41 occupies a framework site, tetrahedral site symmetry is expected for Ti(III) in dehydrated samples. On the other hand, in ETS-4 and ETS-10, the framework titanium is in octahedral coordination. The ground state of Ti(III) with a $3d^1$ configuration is ^2D. When this ion is subjected to a perfect cubic crystalline field from tetrahedral or octahedral coordination, its fivefold degeneracy is lifted into a doublet and a triplet. In a tetrahedral field, the doublet lies lower in energy, while in octahedral coordination the triplet has the lower energy as shown in Fig. 23. An additional trigonal or tetragonal distortion is necessary to lift the degeneracy of the low-lying doublet (tetrahedral) or triplet (octahedral) and is responsible for the g anisotropy and the deviation of g_{av} from the free electron value $g_e = 2.0023$. In a tetragonally distorted tetrahedral field, the g values calculated to first order are as follows (30):

$$g = g_e \text{ and } g_\perp = g_e - 6\lambda/\Delta \text{ (tetragonal compression)}$$
$$g \approx g_e - 8\lambda/\Delta \text{ and } g_e - 2\lambda/\Delta \text{(tetragonal elongation)}$$

Here g is the spin orbit coupling constant and Δ is the energy splitting between the degenerate triplet and doublet levels in a cubic tetrahedral field (Fig. 23b). From the ordering of the g values observed for Ti(III) in TS-1 and TiMCM-41 after γ irradiation, the most likely situation is one of tetragonal compression. However, there are wide variations in the values reported for the ESR parameters of Ti(III) centers in various compounds.

It has been observed that in a trigonal field, Ti(III) in octahedral coordination generally yields a spectrum for which the value of $g_\parallel$ is larger than $g_\perp$ (31). But this is not the case observed in both ETS-4 and ETS-10. The observed ESR signals of Ti(III) in ETS-4 and ETS-10 can be explained on the basis of tetragonal or rhombic distortions to the octahedral crystal field of Ti(III) similar to that observed for several $3d^1$ ions in a rutile structure (32). The anisotropy of the ESR signal of Ti(III) arises by distortion of the cubic field due to displacement of one or both of the axial oxygens or displacement of one or more of the four planar oxygens. The first possibility gives the required tetragonal field. The second possibility produces a crystal field of symmetry lower than tetragonal. The anisotropy can also arise due to distortion caused by strong interaction from nearby cations such as Na^+ or K^+. Thus, upon assuming tetragonally distorted octahedral symmetry for Ti(III) ion in ETS-4, the g values calculated to the first order are $g_\perp \approx g_e - 8\lambda/\Delta$ and $g_\parallel \approx g_e - 2\lambda/\delta$. Using the values for $\lambda = 154\ cm^{-1}$, and the observed g values, the calculated values of energy splitting are $\Delta = 15{,}700\ cm^{-1}$ and $\delta = 2700\ cm^{-1}$.

The fact that Ti(III) in ETS-10 has a rhombic ESR signal with three g components indicates that the crystal symmetry is lower than tetragonal. Thus, the second possibility of distortions caused by displacement of planar oxygens or by interactions from nearby ions seems to be more likely in this case. As a result of this distortion, the degeneracy of the ground-state triplet level is lifted. Assuming a D_{2h} site symmetry for Ti(III) ion in ETS-10, provided the spin orbit interaction is not too high, the g values calculated to the first order are $g_1 = g_e - 8\lambda/\Delta$; $g_2 = g_e - 2\lambda/\delta+$; $g_3 = g_e - 2\lambda/\delta-$. Here, Δ, δ+, and δ- are, respectively, the energy separations of the upper doublet e_g (d_z, d_{xy}), and the middle lying d_{xz} and d_{yz} states from the ground-state $d_{x\text{-}y}$ (Fig. 23a). Substituting the experimentally observed g values into the above expressions, one obtains

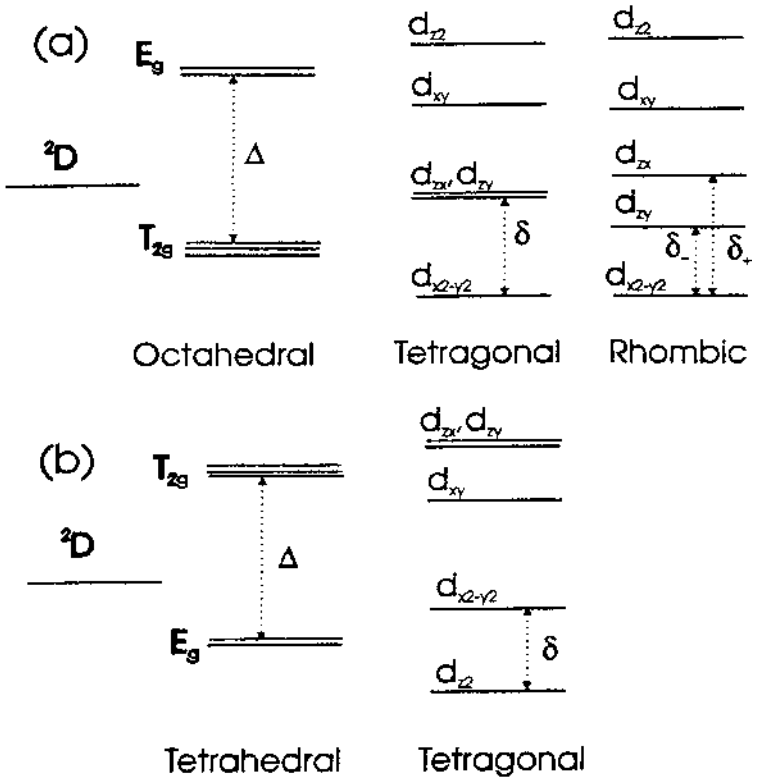

Fig. 23 Energy levels of a $3d^1$ ion in (a) octahedral and (b) tetrahedral cubic fields. (From Ref. 28.)

$\Delta = 23{,}000\ cm^{-1}$, $\delta+ = 3800\ cm^{-1}$, and $\delta- = 2700\ cm^{-1}$. The octahedral field splitting Δ is still predominant, and additional separations of about 1000 wavenumbers among the lower triplet component are enough to explain the observed *g* tensor.

The difference in coordination of titanium in TS-1 and TiMCM-41 compared with ETS-4 and ETS-10 is further reflected by their behaviors toward adsorption of various adsorbates. Upon adsorption of molecules such as D_2O, CH_3OD, and C_2D_4 on TS-1 and TiMCM-41, new ESR signals are observed for Ti(III) suggesting significant modification of the crystal field around this ion by interaction from these molecules. Deuterium electron spin-echo modulation shows that these adsorbates can directly coordinate to Ti(III) in these tetrahedrally coordinated systems. On the other hand, no significant change in the ESR signal for Ti(III) is observed in ETS-10 after adsorption of these molecules. This suggests that there is no direct coordination or strong interaction between Ti(III) and these molecules in ETS-10 where the Ti(III) is octahedrally coordinated. This conclusion is verified by the ESEM measurements on these samples with deuterated adsorbates showing little deuterium modulation.

IV. APPLICATIONS TO PARAMAGNETIC ORGANIC SPECIES

A. Organic Radical Structure

Radicals and radical ions can often be stabilized in the spatially constrained environments of microporous materials. Often a single radical species can be nearly exclusively formed in such environments by photoirradiation or by ionizing radiation (X rays, γ rays, etc.). This allows

determination of the radical structure to a great degree of detail by determination of hyperfine and *g* anisotropies. It is also of interest to determine whether a radical on an oxide surface or in an oxide cage has a slightly different structure and hence different magnetic anisotropy than that in a bulk crystal or frozen solution.

One example is the naphthalene radical cation produced by X irradiation in H-ZSM-5 zeolite with the ESR spectrum shown in Fig. 24. It been studied in detail by ESR, ENDOR, and ESEM (33), and the *g* tensor and ring proton hyperfine tensors were determined. In addition, by using naphthalene-d_8 in H-ZSM-5 the deuterium nuclear quadrupole tensors were determined by ESEM. This determination of the magnetic radical structure facilitated the excellent ESR simulation in Fig. 24. In this case it was found that the radical structure was identical to that in frozen solution.

Related CW ESR studies have focused on the reactions of radiation-produced radical ions in ZSM-5 zeolites. Acetylene radical anion is stabilized in H-ZSM-5 but not in Na-ZSM-5 (34). This is shown by the different spectra in Figs. 25 and 26. Thus, the strength of the electrostatic field within the zeolite can control the reaction pathway. Formation of the hydrocarbon radical anion in zeolite radiolysis is a rare finding and contrasts with results for other unsaturated hydrocarbons adsorbed on H-ZSM-5, for which radical cations only are formed. The ESR spectrum of $HCCH^-$ with an isotropic hyperfine coupling of 65 G in H-ZSM-5 shows the radical anion to be in the cis-bent form.

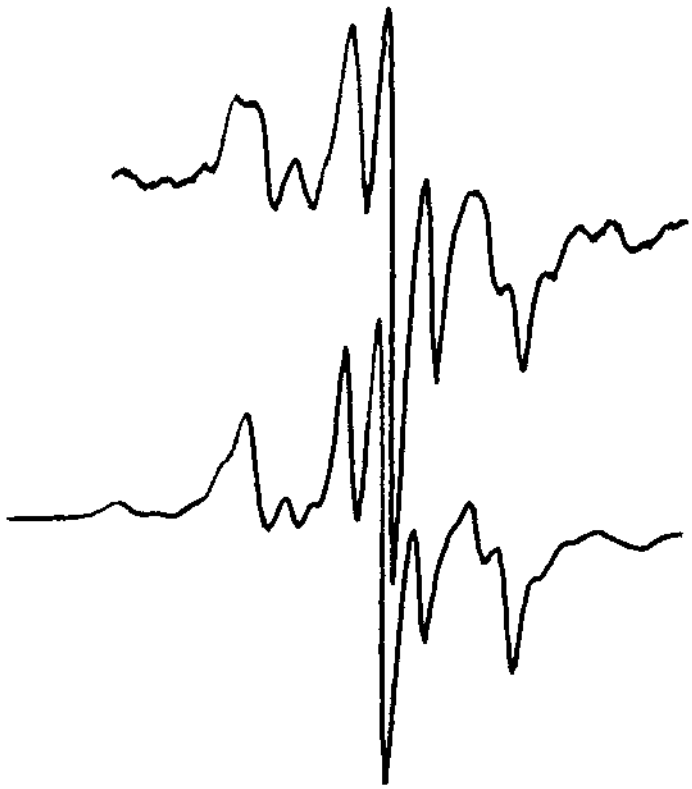

Fig. 24 Comparison of experimental (upper) and simulated (lower) powder ESR spectra of the naphthalene-h_8 radical cation at 77 K in H-ZSM-5 zeolite. (From Ref. 33.)

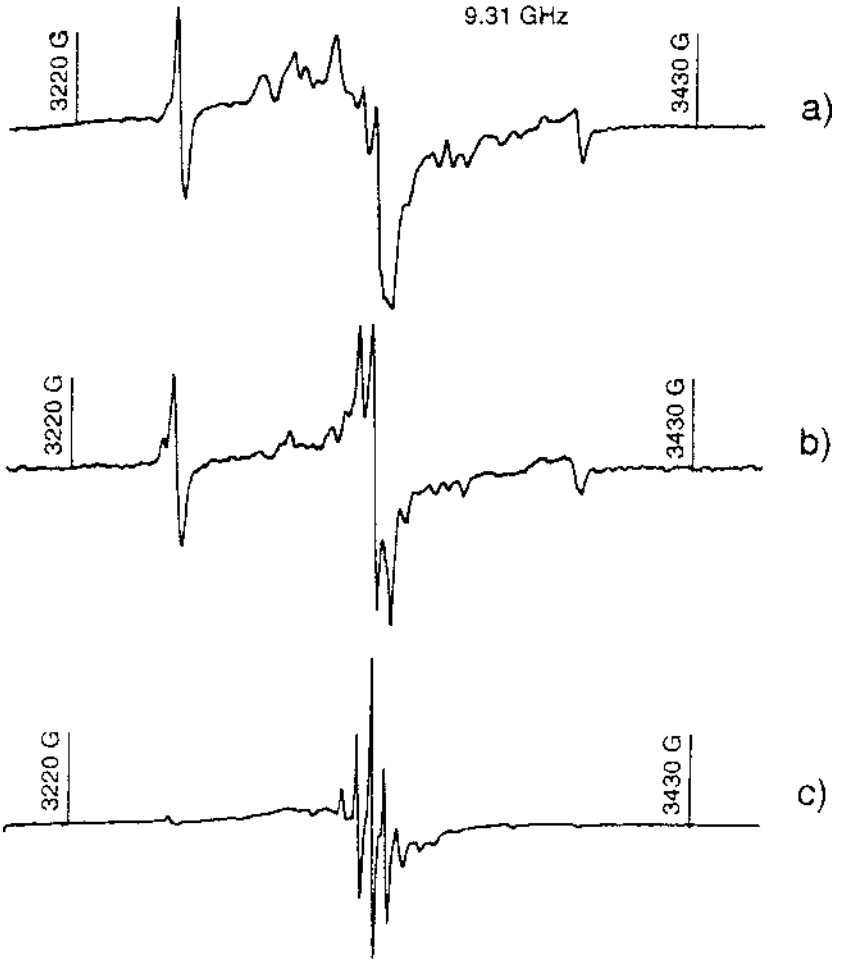

Fig. 25 ESR spectra obtained at 70 K after 77 K γ irradiation of (a) H-ZSM-5(Si/Al = 400), (b) H-ZSM-5(Si/Al = 240), and (c) H-ZSM-5(Si/Al = 50) containing 0.1% acetylene. (From Ref. 34.)

The benzene radical cation was observed in both acetylene-loaded H-ZSM-5 and Na-ZSM-5 zeolites. This radical cation can be formed via two mechanisms. In Na-ZSM-5 it can be formed by ionization of acetylene and subsequent ion–molecule reactions with neutral acetylene molecules. In H-ZSM-5 Brønsted acid sites can convert acetylene to trimers (benzene), which are ionized upon radiolysis.

B. Organic Radical Reorientation

Molecular reorientation of organic radicals in zeolites can also be studied not only by ESR lineshape analysis vs. temperature but also by the temperature dependence of the electron phase memory time measured by electron spin-echo decay. This has been applied to the phenalenyl radical in X and Y zeolites with various alkali metal ions (35). There is a good correspondence between the temperature dependencies of the electron spin phase memory time and the CW ESR spectra. Both display evidence of a thermal activation from a stationary, nonrotating molecular state to a low-temperature state of in-plane rotation. The rate of in-plane rotation is an activated

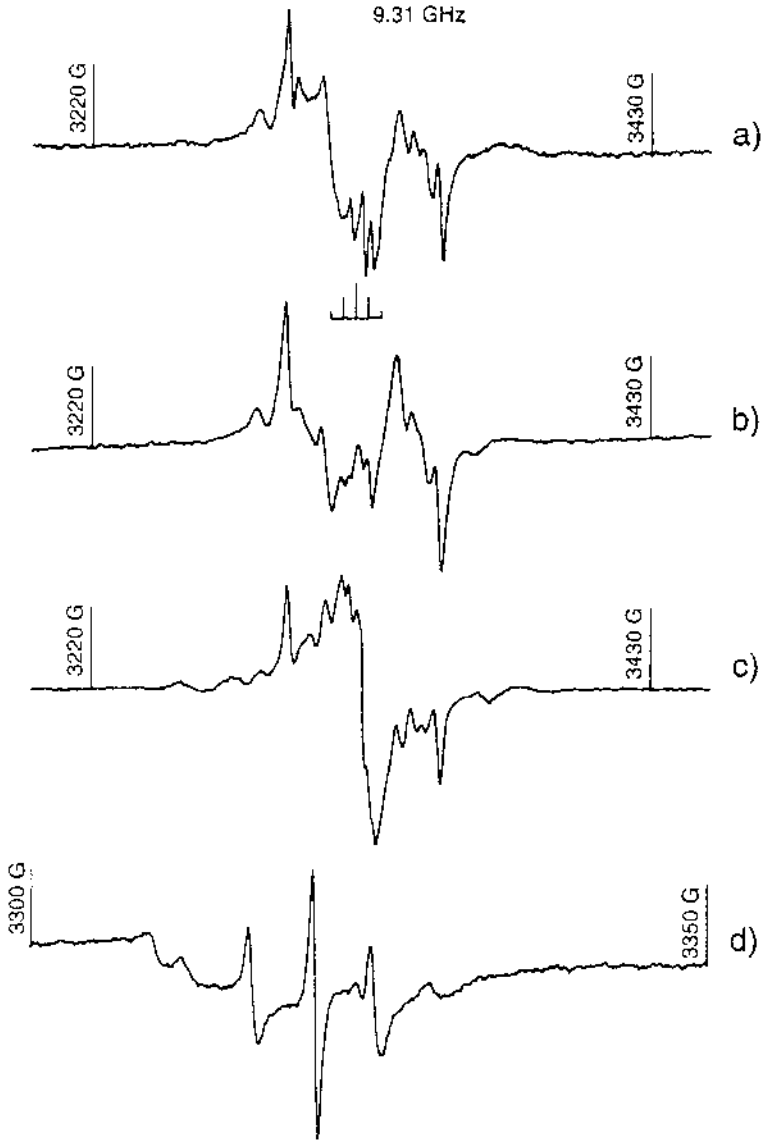

Fig. 26 ESR spectra obtained at 70 K after 77 K γ irradiation of (a) Na-ZSM-5(Si/Al = 1000), (b) Na-ZSM-5(Si/Al = 170), and (c) Na-ZSM-5(Si/Al = 40) containing 0.1% acetylene. Part (d) shows the ESR spectrum obtained at 130 K after 77 K γ irradiation of Na-ZSM-5(Si/Al = 40) containing 0.1% acetylene. (From Ref. 34.)

process with a larger activation energy for K-X vs. Na-X, which correlates with cation size. The rotation appears to be about an axis along which the half-filled, nonbonding π orbital interacts with the exchanged cation in the alpha cage. Both CW and pulsed ESR also show a higher temperature activation from the in-plane rotating state to an effectively isotropic state of rotation in which the phenalenyl-cation bond is thought to be broken. The strength of the phenalenyl-cation bonding decreases with increasing cation size, and the peripheral repulsion or crowding of phenalenyl also increases with cation size.

Related studies using only ESR lineshape analysis have dealt with NO_2 rotation in X and Y zeolites which differ in the Si/Al ratio and consequently the internal electrostatic field (36). ESR spectra of NO_2 adsorbed on X and Y zeolites were observed in the temperature range 77–346 K. Based on ESR spectral simulation using a Brownian diffusion model, the motional dynamics of NO_2 adsorbed on zeolites was analyzed quantitatively. For X zeolite, it was found that the ESR spectra for adsorbed NO_2 below 100 K are near the rigid motional limit. At higher temperature, the average rotational correlation time decreased from 1.7×10^{-9} s at 230 K to 7.5×10^{-10} s at 325 K. For Y zeolite, the temperature-dependent ESR spectra for adsorbed NO_2 show more axially symmetrical motion about the axis through the center of mass and parallel to the two oxygens in comparison with X zeolite. Also, the activation energy for rotational diffusion is much smaller in Y zeolite than in X zeolite.

The motional dynamics of NO_2 adsorbed on Na-ZSM-5 with different Si/Al ratios to change the internal electrostatic field was also studied by the temperature dependence (3 - 160 K) of the ESR spectral lineshape (37). The lineshape changes were quantitatively analyzed with slow-motion ESR theory. Computer analysis with Heisenberg spin exchange reveals that the spin exchange rate of NO_2 below 160 K increases as the Si/Al ratio is increased. It was concluded that the difference in the amount of Na^+, which depends on the Si/Al ratio, is the main reason for the variation in spin exchange rates. This is the same trend found in X vs. Y zeolite in which the motional activation energy decreases with increasing Si/Al ratio.

REFERENCES

1. L Kevan. Acct Chem Res 20:1–7, 1987.
2. L Kevan. In: L Kevan, MK Bowman, eds. Modern Pulsed and Continuous-Wave Electron Spin Resonance. New York: Wiley, 1990, Chapter 5, pp 231–266.
3. L Kevan, MK Bowman, PA Narayana, RK Boeckman, VF Yudanov, Yu D Tsvetkov. J Chem Phys 63:409–416, 1975.
4. T Ichikawa, L Kevan, MK Bowman, SA Dikanov, Yu D Tsvetkov. J Chem Phys 71:1167–1174, 1979.
5. WB Mims. Phys Rev B 5:2409–2419, 1972; Phys Rev B 6:3543–3545, 1972.
6. SA Dikanov, AA Shubin, VN Parmon. J Magn Reson 42:474–487, 1981.
7. M Anderson, L Kevan. J Chem Phys 86:1–6, 1987.
8. M Anderson, L Kevan. J Chem Soc Faraday Trans I 83:3505–3512, 1987.
9. M Romanelli, M Narayana, L Kevan. J Chem Phys 80:4044–4050, 1984.
10. AA Shubin, SA Dikanov. J Magn Reson 52:1–12, 1983.
11. AA Shubin, SA Dikanov. J Magn Reson 64:185–193, 1985.
12. M Heming, M Narayana, L Kevan. J Chem Phys 83:1478–1484, 1985.
13. P Hofer, A Grupp, H Nebenfur, M Mehring. Chem Phys Lett 132:279–282,1986.
14. WB Mims. Proc Royal Soc A 283:452–457, 1965.
15. ER Davies. Phys Lett A 47A:1–2, 1974.
16. D Goldfarb. In: BM Weckhuysen, P Van Der Voort, G Catana, eds. Spectroscopy of Transition Metal Ions on Surfaces. Leuven, Belgium: Leuven University Press, 2000, pp 93–133.
17. MW Anderson, L Kevan. J Phys Chem 91:1850–1856, 1987.
18. L Kevan. Pure Appl Chem 64:781–788, 1992.
19. M Narayana, L Kevan. J Am Chem Soc 103:5729–5733, 1981.
20. MW Anderson, L Kevan. J Phys Chem 91:4174–4179, 1987.
21. T Ichikawa, L Kevan. J Am Chem Soc 105:402–406 ,1983.
22. AK Ghosh, L Kevan. J Am Chem Soc 10:8044–8050, 1988.
23. JS Bass, L Kevan. J Phys Chem 94:1483–1489, 1990.
24. T Wasowicz, SJ Kim, SB Hong, L Kevan. J Phys Chem 110:15954–15960, 1996.
25. JS Yu, V Kurshev, L Kevan. J Phys Chem 98:10225–10228, 1994.

26. M Hartmann, N Azuma, L Kevan. J Phys Chem 99:10988–10994, 1995.
27. L Kevan. J Phys Chem 85:1628–1636, 1981.
28. AM Prakash, L Kevan. In: MMJ Treacy, B Marcus, ME Bisher, JB Higgins, eds. Proceedings of the 12th International Zeolite Conference, Vol. 4. Warrendale, PA: Materials Research Society, 1999, pp 2825–2832.
29. YM Kim, DE Reardon, PJ Bray. J Chem Phys 48:3396–3402, 1968.
30. JA Weil, JR Bolton, JE Wertz. Electron Paramagnetic Resonance. New York:Wiley, 1994, Chapter 8, pp 213–238.
31. HM Gladney, JD Swalen. J Chem Phys 42:1999–2010, 1965.
32. PH Kasai. Phys Letts 7:5–6, 1963.
33. LA Eriksson, NP Benetis, A Lund, M Lindgren. J Phys Chem 101:2390–2396, 1997.
34. EA Piocos, DW Werst, AD Trifunac, LA Eriksson. J Phys Chem 100:8408–8417, 1996.
35. DC Doetschman, DW Dwyer, JD Fox, CK Frederick, S Scull, GD Thomas, SG Utterback. J Wei Chem Phys 185:343–356, 1994.
36. H Yahiro, M Shiotani, JH Freed, M Lingren, A Lund. In: HK Beyer,HG Karge, JB Nagy, eds. Catalysis by Microporous Materials. New York:Elsevier, 1995, pp 673–680.
37. H Li, A Lund, M Lingren, E Sagstuen, H Yahiro. Chem Phys Lett 271:84–89,1997.